Monthly Notices of the ROYAL ASTRONOMICAL SOCIETY

MNRAS **521,** 5207–5223 (2023) https://doi.org/10.1093/mnras/stad864
Advance Access publication 2023 March 23

Type Ia supernovae SN 2013bz, PSN J0910 + 5003, and ASASSN-16ex: similar to 09dc-like?

S. Tiwari,[1★] N. K. Chakradhari,[1,2★] D. K. Sahu,[3★] G. C. Anupama [3], B. Kumar [4] and K. R. Sahu[1]

[1]*School of Studies in Physics & Astrophysics, Pt. Ravishankar Shukla University, Raipur 492010, India*
[2]*Centre for Mega Projects in Multiwavelength Astronomy, Pt. Ravishankar Shukla University, Raipur 492010, India*
[3]*Indian Institute of Astrophysics, Koramangala, Bangalore 560034, India*
[4]*Aryabhatta Research Institute of observational sciencES (ARIES), Manora Peak, Nainital 263001, India*

Accepted 2023 March 14. Received 2023 March 14; in original form 2022 November 4

ABSTRACT

We present optical photometric and spectroscopic studies of three supernovae (SNe): SN 2013bz, PSN J0910 + 5003, and ASASSN-16ex (SN 2016ccj). UV–optical photometric data of ASASSN-16ex obtained with the *Swift* Ultraviolet/Optical Telescope (UVOT) are also analysed. These objects were initially classified as 09dc-like type Ia SNe. The decline-rate parameters ($\Delta m_{15}(B)_{\rm true}$) are derived as 0.92 ± 0.04 (SN 2013bz), 0.70 ± 0.05 (PSN J0910 + 5003), and 0.73 ± 0.03 (ASASSN-16ex). The estimated *B*-band absolute magnitudes at maximum, −19.61 ± 0.20 mag for SN 2013bz, −19.44 ± 0.20 mag for PSN J0910 + 5003, and −19.78 ± 0.20 mag for ASASSN-16ex, indicate that all three objects are relatively bright. The peak bolometric luminosities for these objects are derived as $\log L_{\rm bol}^{\rm max} = 43.38 \pm 0.07$, 43.26 ± 0.07, and 43.40 ± 0.06 erg s^{-1}, respectively. The spectral and velocity evolution of SN 2013bz is similar to that of a normal SN Ia, hence it appears to be a luminous, normal type Ia supernova. On the other hand, the light curves of PSN J0910 + 5003 and ASASSN-16ex are broad and exhibit properties similar to 09dc-like SNe Ia. Their spectroscopic evolution shows similarity with 09dc-like SNe: strong C II lines are seen in the pre-maximum spectra of these two events. Their photospheric velocity evolution is similar to SN 2006gz. Further, in the UV bands, ASASSN-16ex is very blue, like other 09dc-like SNe Ia.

Key words: techniques: photometric – techniques: spectroscopic – supernovae: general – supernovae: individual: SN 2013bz – supernovae: individual: PSN J0910 + 5003 – supernovae: individual: ASASSN-16ex.

1 INTRODUCTION

Thermonuclear supernovae are an important class of supernovae (SNe): the progenitors are low-mass stars found in elliptical as well as spiral galaxies. They are commonly known as Type Ia SNe (SNe Ia) and populate the brighter side of the luminosity distribution of SNe. Most SNe Ia, referred to as 'normal SNe Ia', display uniform spectral and light-curve properties. Their luminosity is correlated with the width of their light curve (Phillips 1993; Phillips et al. 1999) and hence they are considered standardizable candles. This uniformity and high luminosity make them a vital probe for studying cosmic evolution (Riess et al. 1998; Perlmutter et al. 1999). SNe Ia are the primary source of iron-group elements (IGEs) and hence play an important role in enriching the interstellar medium (ISM) with IGEs (Matteucci & Greggio 1986; Matteucci et al. 2009; Nomoto, Kobayashi & Tominaga 2013).

Our understanding of the progenitor and explosion mechanism giving rise to these events still needs to be completed. From the theoretical and observational work, it is inferred that thermonuclear disruption of a carbon–oxygen (C/O) white dwarf (WD) in a binary system results in a Type Ia explosion (Hoyle & Fowler 1960; see Maoz, Mannucci & Nelemans 2014; Jha, Maguire & Sullivan 2019 for reviews). There are two possible progenitor models suggested for a WD to explode. In the first one, a WD accretes matter from a non-degenerate star, known as the single-degenerate (SD) model (Whelan & Iben 1973). In the double-degenerate (DD) model, the explosion results from the merger of two WDs (Iben & Tutukov 1984; Webbink 1984). Most SNe Ia are considered to be an explosion of a Chandrasekhar-mass WD (Mazzali et al. 2007) via delayed detonation (Khokhlov 1991). However, if the accumulated material is He-rich, the explosion can occur at a sub-Chandrasekhar mass through double detonation. With sufficiently rapid He accretion on the surface of a C/O WD, a detonation is first initiated within the helium layer. The emanating shock wave propagates through the WD and triggers carbon detonation at the centre of the WD (Woosley & Weaver 1994; Woosley & Kasen 2011; Ruiter et al. 2014; Tanikawa, Nomoto & Nakasato 2018). The donor star could be either a non-degenerate He star (SD channel), another C/O WD with He in the outer layer, or a He WD (DD channel). This mechanism can explain normal and fast-declining SNe Ia of different brightness distributions (Pakmor et al. 2013). Currently, it is difficult to identify which SN results from which channel (see Livio & Mazzali 2018; Wang 2018; Soker 2019; Ruiter 2020, for reviews).

With the increasing number of well-studied SNe Ia, it became clear that there is a considerable spread in the luminosity of SNe Ia. There are objects populating both the higher and lower luminosity end of normal objects (Li et al. 2011). Some have extreme properties

★ E-mail: shrutikatiwari7@gmail.com (ST); nkchakradhari@gmail.com (NC); dks@iiap.res.in (DS)

that are significantly different from the normal class (Taubenberger 2017).

A small group of extreme/peculiar objects (e.g. SN 2003fg: Howell et al. 2006, SN 2006gz: Hicken et al. 2007; Maeda et al. 2009, SN 2007if: Scalzo et al. 2010; Yuan et al. 2010, SN 2009dc: Yamanaka et al. 2009; Silverman et al. 2011; Taubenberger et al. 2011) are known to have broad light curves and generally have a brighter peak luminosity than predicted by their decline rate (Phillips et al. 1999). In most of these, the ejecta mass inferred through simple analytic modelling, and hence the progenitor mass, is found to be higher than the Chandrasekhar mass, so they are termed super-Chandrasekhar SNe Ia or 03fg/09dc-like SNe Ia. They are UV blue and bright in the early phase. Near-maximum spectra of 09dc-like SNe are similar to those of normal events, characterized by intermediate-mass elements (IMEs) but with relatively narrow/weak spectral features. The photospheric velocity is found to be low, with slow evolution. The presence of unburned carbon in the ejecta is often seen in the pre-maximum spectral sequence.

The light-curve and spectral evolution of SN 2012dn were similar to those of 09dc-like objects. However, it had weak carbon, relatively strong features from IMEs, and was fainter compared with other 09dc-like SNe Ia (Chakradhari et al. 2014; Brown et al. 2014b; Parrent et al. 2016; Yamanaka et al. 2016; Taubenberger et al. 2019). Now it appears that even this group (with some new members, e.g. ASASSN-15pz, LSQ14fmg, ASASSN-15hy, and SN 2020esm) exhibits diverse observational properties (Chen et al. 2019; Hsiao et al. 2020; Ashall et al. 2021; Lu et al. 2021; Dimitriadis et al. 2022). The luminous Type Ia SNe SN 2020hvf (Jiang et al. 2021), SN 2021zny (Dimitriadis et al. 2023), and SN 2022ilv (Srivastav et al. 2023) were also found to be similar to 09dc-like SNe, having broad light curves and strong carbon features in the early spectra. Early excess emission was seen in these SNe within a few hours of the explosion.

In this work, we present a detailed photometric and spectroscopic study of three SNe Ia: SN 2013bz, PSN J0910 + 5003, and ASASSN-16ex. They were initially classified as 09dc-like SNe Ia.

The Catalina Real-time Transient Survey discovered SN 2013bz on 2013 April 21.28 (time is always in UT) and classified it as a normal Type Ia SN around the maximum. However, it was noted that it could also be an overluminous event (Howerton et al. 2013). Ochner et al. (2013) reported that the spectrum obtained on 2013 May 4.96 matched well with SNe 2006gz/09dc. SN was located at RA = $13^{h}26^{m}51^{s}.32$, Dec. = $-10^{\circ}01'32''.2$ (J2000), 7.5 arcsec east and 5.8 arcsec south of the nucleus of host galaxy PGC 170 248 (Fig. 1, top).

The Italian SNe Search Project discovered PSN J0910 + 5003 on 2015 November 8.17 (Ciabattari, Mazzoni & Petroni 2015). The object was located at RA = $09^{h}10^{m}08^{s}.85$, Dec. = $50^{\circ}03'39''.6$ (J2000), 9 arcsec east and 8 arcsec north of the centre of host galaxy UGC 4812 (Fig. 1, middle). A spectrum obtained on 2015 November 09.13 matched well with SN 2009dc about ten days before maximum light (Tomasella et al. 2015).

The All-Sky Automated Survey for SNe discovered ASASSN-16ex (SN 2016ccj) on 2016 May 03.43 (Kiyota et al. 2016). The SN was located at RA = $17^{h}10^{m}23^{s}.92$, Dec. = $26^{\circ}23'47''.89$ (J2000), 1.9 arcsec south and 3.8 arcsec east from the centre of the host galaxy SDSS J171023.63 + 262350.3 (Fig. 1, bottom). Spectra obtained by Piascik & Steele (2016) and Tomasella et al. (2016) matched well with SNe 2009dc/06gz, about 10–12 days before maximum. Prominent C II lines (6580 Å and 7234 Å) were also detected in the spectra. The UV colours and absolute magnitudes of ASASSN-

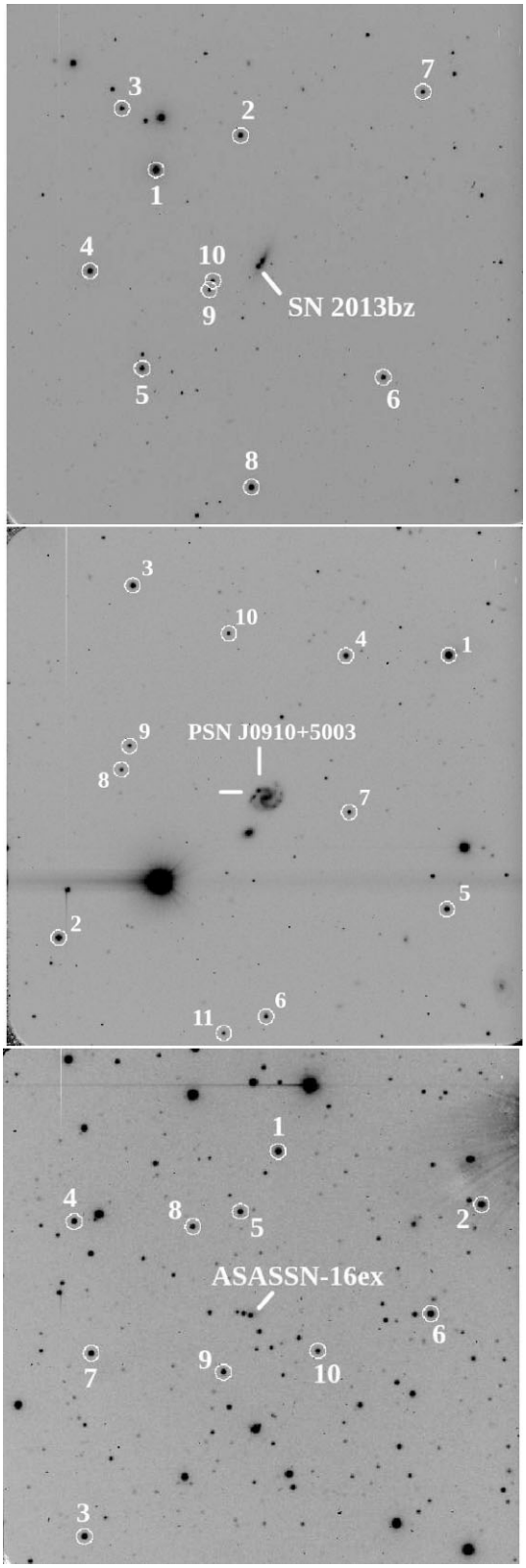

Figure 1. Identification chart for SNe 2013bz (top), PSN J0910 + 5003 (middle), and ASASSN-16ex (bottom). The stars used as secondary standards are marked. North is up and east to the left. The field of view is 10 × 10 arcmin^2 each. Images were obtained using the 2-m HCT, IAO, Hanle, India.

16ex were found to be blue and bright, similar to 09dc-like events (Brown & Milne 2016).

The layout of this work is as follows. Observations and data reduction techniques are presented in Section 2. The light curves and colour curves are discussed in Section 3. Physical parameters of the SNe, e.g. peak absolute magnitude, bolometric luminosity and mass of ^{56}Ni, etc., are estimated in Section 4. The spectral evolution and a comparison with other well-studied SNe Ia are presented in Section 5. The results are discussed and summarized in Section 6. Throughout this work, we adopt the Vega magnitude system.

2 OBSERVATIONS AND DATA REDUCTION

2.1 Imaging

SN 2013bz, PSN J0910 + 5003, and ASASSN-16ex were monitored using the 2-m Himalayan Chandra Telescope (HCT) of the Indian Astronomical Observatory (IAO[1]), Hanle, India. Observations were carried out in Bessell's *UBVRI* bands using the Himalaya Faint Object Spectrograph Camera (HFOSC).

Photometric monitoring of SN 2013bz started on 2013 May 2 and continued until 2013 July 4. Standard star fields PG 1633 + 099, PG 2213–006, PG 1525–71, and PG 1323–086 from Landolt (1992) were observed on six photometric nights (2013 May 2, 14, 21, and 30, June 4, and July 4) to calibrate a sequence of secondary standards in the SN field.

Photometric observations of PSN J0910+5003 were carried out from 2015 November 10–2016 March 13. Standard star fields PG 0231+051, PG 0918+029, PG 2213–006, PG 1047 + 003, and PG 0942–029 were observed on five photometric nights (2015 November 17, 20, and 28, 2020 December 1, and 2021 March 1).

Photometric monitoring of ASASSN-16ex began on 2016 May 7 and continued until 2016 September 17. Standard star fields PG 1633+099, SA 110, PG 2213–006, PG 0231+051, and PG 2331 + 055 were observed on seven photometric nights (2016 May 14, June 3, 18, and 26, July 6 and 31, and October 4). Several bias frames and twilight flats necessary for pre-processing were also obtained during each observation.

The observed data were processed in a standard manner using the Image Reduction and Analysis Facility (IRAF[2]) package. The observed Landolt standards were used to calibrate a sequence of secondary standards in the SNe field, following the procedures of Chakradhari et al. (2014) and Chakradhari, Sahu & Anupama (2019). The mean *UBVRI* magnitudes of secondary standards in the field of SN 2013bz, PSN J0910 + 5003 and ASASSN-16ex (marked in Fig. 1), are listed in Table 1.

The host galaxy background contaminated SN 2013bz and PSN J0910 + 5003 significantly. Template subtraction photometry was performed for these SNe to remove the contribution from the host to the SN flux. Deep *UBVRI* template frames of PGC 170 248 and UGC 4812 fields were obtained in good seeing conditions with the same instrumental setup on 2016 March 15 and 2021 March 1, respectively. Template image subtraction was performed in a standard manner using the IRAF *cl*-script. In the template-subtracted frame, aperture photometry was performed on the SN and calibrated differentially with respect to the secondary standards. The estimated magnitudes of SN 2013bz and PSN J0910 + 5003 are listed in Table 2.

For ASASSN-16ex, profile-fitting photometry was used. The fitting radius was chosen close to the full width at half-maximum (FWHM) of the stellar profile. A correction factor was obtained from the difference between the aperture and profile-fitting magnitudes using bright field stars. This correction factor was applied to the SN magnitude derived using profile fitting, which was then calibrated differentially with respect to the secondary standards in the field. The derived magnitudes of ASASSN-16ex are listed in Table 2. The magnitudes presented in this work are not *K*-corrected.

2.1.1 *UV–optical photometry of ASASSN-16ex using* Swift *UVOT.*

ASASSN-16ex was also observed with the Ultraviolet/Optical Telescope (UVOT: Roming et al. 2005) onboard the Neil Gehrels *Swift* Observatory. Raw imaging data in three broad-band UV filters (*uvw*2: 1928 Å, *uvm*2: 2246 Å, *uvw*1: 2600 Å) and three broad-band optical filters (*u*: 3465 Å, *b*: 4392 Å, *v*: 5468 Å) were accessed from the *Swift* database. Data processing was done using various packages available in the High Energy Astrophysics Software (HEASOFT[3]), following methods outlined in Poole et al. (2008), Brown et al. (2009, 2014a), and Breeveld et al. (2011). The UV–optical magnitudes of ASASSN-16ex are listed in Table 3.

2.2 Spectroscopy

Medium-resolution (∼7 Å) spectra of SN 2013bz, PSN J0910 + 5003, and ASASSN-16ex were obtained using the HFOSC-HCT. Two grisms, Gr7 (3500–7000 Å) and Gr8 (5200–9200 Å), were used to cover the optical wavelength range. A log of spectroscopic observations is given in Table 4. Besides bias and flat frames, spectra of FeNe and FeAr arc lamps were taken for wavelength calibration. Spectra of spectrophotometric standards were obtained to correct for the instrumental response.

Spectroscopic data were reduced using IRAF in a standard manner, as discussed in Chakradhari et al. (2014; 2019). The final spectra were corrected for reddening (refer to Section 4.1) and redshift using $z = 0.019$ for SN 2013bz (source NED), $z = 0.034$ for PSN J0910 + 5003 (source NED), and $z = 0.04$ for ASASSN-16ex (Foley et al. 2018).

3 LIGHT CURVES AND COLOUR CURVES

The estimated magnitudes of SN 2013bz, PSN J0910 + 5003, and ASASSN-16ex are plotted in Figs 2, 3, and 4, respectively. UV–optical data of ASASSN-16ex from *Swift* UVOT are also plotted in Fig. 4. In order to understand the characteristics of these SNe, we derived various photometric parameters from their light curves, which are listed in Tables 5 and 6.

Our observation of SN 2013bz started in the post-maximum phase; hence we used max-model from the SNooPy (Burns et al. 2011) package to fit templates and derive light-curve parameters. The best-matching template light curves are overplotted on to the observed light curves (Fig. 2). SN 2013bz reached maximum brightness in the *B* band on JD 245 6409.5 ± 0.8 with an apparent brightness of 15.71 ± 0.04 mag. Similarly to normal and 91T-like SNe Ia, in SN 2013bz the maxima in *U* and *I* bands precede, and those in the *V* and *R* bands follow, the *B*-band maximum (refer to Table 5). The decline in the *B*-band brightness 15 days after the maximum is estimated as $\Delta m_{15}(B) = 0.91 \pm 0.04$ mag and $\Delta m_{15}(B)_{\rm true} = 0.92 \pm 0.04$

[1] https://www.iiap.res.in/?q = iao.htm
[2] https://iraf-community.github.io/
[3] https://heasarc.gsfc.nasa.gov/docs/software/heasoft/

Table 1. Magnitudes of secondary standards (marked in Fig. 1) in the fields of SN 2013bz, PSN J0910 + 5003, and ASASSN-16ex.

ID	*U*	*B*	*V*	*R*	*I*
			SN 2013bz		
1	14.34 ± 0.02	14.22 ± 0.03	13.51 ± 0.02	13.20 ± 0.03	12.81 ± 0.02
2	15.64 ± 0.02	15.61 ± 0.03	14.92 ± 0.02	14.60 ± 0.02	14.18 ± 0.02
3	15.60 ± 0.02	15.78 ± 0.03	15.16 ± 0.02	14.85 ± 0.02	14.43 ± 0.01
4	14.92 ± 0.01	15.08 ± 0.03	14.47 ± 0.02	14.18 ± 0.02	13.78 ± 0.02
5	15.20 ± 0.01	15.36 ± 0.02	14.75 ± 0.02	14.46 ± 0.02	14.06 ± 0.01
6	16.51 ± 0.03	16.28 ± 0.02	15.52 ± 0.02	15.17 ± 0.02	14.73 ± 0.02
7	17.14 ± 0.05	16.63 ± 0.02	15.73 ± 0.02	15.30 ± 0.02	14.77 ± 0.01
8	15.66 ± 0.03	15.36 ± 0.02	14.54 ± 0.02	14.19 ± 0.03	13.71 ± 0.02
9	17.65 ± 0.05	16.92 ± 0.03	15.96 ± 0.02	15.50 ± 0.02	14.98 ± 0.01
10	16.76 ± 0.03	16.74 ± 0.02	16.05 ± 0.02	15.73 ± 0.02	15.31 ± 0.02
			PSN J0910 + 5003		
1	14.43 ± 0.04	14.51 ± 0.04	13.94 ± 0.02	13.59 ± 0.02	13.35 ± 0.02
2	16.11 ± 0.04	15.80 ± 0.02	15.02 ± 0.01	14.56 ± 0.02	14.17 ± 0.04
3	17.58 ± 0.01	16.50 ± 0.04	15.39 ± 0.02	14.73 ± 0.02	14.16 ± 0.01
4	17.44 ± 0.01	16.61 ± 0.04	15.62 ± 0.03	15.05 ± 0.02	14.57 ± 0.02
5	17.02 ± 0.04	16.49 ± 0.04	15.62 ± 0.02	15.12 ± 0.02	14.66 ± 0.03
6	19.10 ± 0.05	18.06 ± 0.04	16.92 ± 0.03	16.29 ± 0.03	15.73 ± 0.03
7	19.57 ± 0.08	18.54 ± 0.03	17.04 ± 0.03	16.12 ± 0.01	15.25 ± 0.03
8	18.65 ± 0.01	18.19 ± 0.04	17.32 ± 0.02	16.86 ± 0.04	16.44 ± 0.04
9	19.90 ± 0.02	18.92 ± 0.03	17.45 ± 0.02	16.36 ± 0.03	15.01 ± 0.03
10	19.21 ± 0.02	18.52 ± 0.03	17.51 ± 0.03	16.93 ± 0.03	16.38 ± 0.03
11	19.42 ± 0.01	18.54 ± 0.08	17.51 ± 0.04	16.87 ± 0.04	16.27 ± 0.04
			ASASSN-16ex		
1	15.91 ± 0.02	15.89 ± 0.03	15.21 ± 0.02	14.84 ± 0.02	14.50 ± 0.02
2	16.31 ± 0.03	16.04 ± 0.04	15.22 ± 0.02	14.74 ± 0.02	14.29 ± 0.03
3	16.36 ± 0.02	16.37 ± 0.04	15.70 ± 0.02	15.33 ± 0.03	14.98 ± 0.03
4	16.73 ± 0.04	16.70 ± 0.03	16.01 ± 0.02	15.64 ± 0.02	15.28 ± 0.03
5	16.88 ± 0.04	16.88 ± 0.03	16.19 ± 0.02	15.81 ± 0.01	15.44 ± 0.02
6	16.89 ± 0.02	16.30 ± 0.04	15.38 ± 0.02	14.85 ± 0.01	14.36 ± 0.02
7	17.02 ± 0.05	16.89 ± 0.04	16.13 ± 0.02	15.72 ± 0.02	15.33 ± 0.02
8	17.00 ± 0.05	17.35 ± 0.02	16.79 ± 0.02	16.44 ± 0.02	16.09 ± 0.02
9	17.15 ± 0.05	17.09 ± 0.04	16.41 ± 0.02	16.03 ± 0.02	15.65 ± 0.02
10	17.36 ± 0.03	17.70 ± 0.03	17.16 ± 0.02	16.83 ± 0.01	16.49 ± 0.03

Note. All magnitudes are in the Vega system.

(Phillips et al. 1999; Folatelli et al. 2010). The estimated decline-rate parameter for SN 2013bz is smaller than that for normal SNe Ia, suggesting it to be a luminous event (Phillips et al. 1999). The decline rates in other bands are listed in Table 6. A distinct and pronounced secondary peak in the *I*-band light curve, a characteristic feature of normal and 91T-like SNe Ia, is seen at ∼ + 30 d. A small hump is also seen in the *R*-band light curve at a similar phase. The *I*-band secondary maximum timing agrees with its derived $\Delta m_{15}(B)$ (Hamuy et al. 1996; Kasen 2006; Folatelli et al. 2010). The light curves of a typical Ia event SN 2003du (Anupama et al. 2005) are also plotted along with SN 2013bz in Fig. 2. From a quick comparison, it is apparent that the light curves of SN 2013bz are similar to those of a normal Ia event.

In the case of PSN J0910+5003 and ASASSN-16ex, our observations started well before the maximum phase. We fitted a cubic spline function to the data points around the maximum to estimate the date of the maximum and magnitude at maximum. PSN J0910 + 5003 reached maximum brightness in the *B* band on JD 245 7347.0 ± 0.6 with 17.13 ± 0.04 mag. The decline-rate parameter is estimated as $\Delta m_{15}(B) = 0.69 \pm 0.04$ and $\Delta m_{15}(B)_{\rm true} = 0.70 \pm 0.04$. The decline rate of PSN J0910+5003 is slower than that of normal SNe Ia. The important photometric parameters derived for PSN J0910 + 5003 are listed in Table 6.

ASASSN-16ex reached maximum light on JD 245 7523.25 ± 0.5 with 16.84 ± 0.03 mag. The decline-rate parameter for ASASSN-16ex is estimated as $\Delta m_{15}(B) = 0.72 \pm 0.03$ and $\Delta m_{15}(B)_{\rm true} = 0.73 \pm 0.03$. The important light-curve parameters derived for ASASSN-16ex (including data from UVOT) are listed in Table 6.

The slow declining nature of PSN J0910 + 5003 and ASASSN-16ex is obvious from an immediate comparison of their light curves (refer to Figs 3 and 4) with the light curves of the normal Type Ia SN 2003du. It is interesting to note that, for both PSN J0910 + 5003 and ASASSN-16ex, $\Delta m_{15}(B)$ is close to that of 09dc-like SNe Ia: SN 2009dc ($\Delta m_{15}(B) = 0.71$; Taubenberger et al. 2011), SN 2007if ($\Delta m_{15}(B) = 0.71$; Scalzo et al. 2010), SN 2006gz ($\Delta m_{15}(B) = 0.69$; Hicken et al. 2007), ASASSN-15pz ($\Delta m_{15}(B) = 0.67$; Chen et al. 2019), and ASASSN-15hy ($\Delta m_{15}(B) = 0.72$; Lu et al. 2021).

Timings of maximum brightness in *U*, *V*, *R*, and *I* bands for PSN J0910 + 5003, ASASSN-16ex, and some other well-studied SNe Ia are listed in Table 5. In PSN J0910 + 5003, the *I*-band peak appears much later (6 d) than that of the *B* band, similar to 09dc-like SNe Ia. In contrast, the *I*-band peak in ASASSN-16ex follows the trend of normal SNe Ia.

In Fig. 5, *BVRI* light curves of SN 2013bz, PSN J0910 + 5003, and ASASSN-16ex are compared with those of well-studied normal

Table 2. Optical *UBVRI* photometry of SN 2013bz, PSN J0910 + 5003, and ASASSN-16ex with HCT.

Date	JD	Phase[a]	*U*	*B*	*V*	*R*	*I*
				SN 2013bz			
02/05/2013	245 6415.22	5.72	15.49 ± 0.02	15.90 ± 0.01	15.55 ± 0.01	15.52 ± 0.01	15.72 ± 0.01
03/05/2013	245 6416.16	6.66		15.93 ± 0.01	15.54 ± 0.01	15.54 ± 0.01	15.79 ± 0.03
05/05/2013	245 6418.18	8.68		16.09 ± 0.01	15.65 ± 0.01	15.66 ± 0.01	15.94 ± 0.02
06/05/2013	245 6419.22	9.72	15.77 ± 0.01	16.11 ± 0.01	15.71 ± 0.01	15.74 ± 0.02	16.01 ± 0.02
08/05/2013	245 6421.24	11.74	15.94 ± 0.02	16.30 ± 0.02	15.83 ± 0.01	15.96 ± 0.01	16.19 ± 0.01
14/05/2013	245 6427.13	17.63		16.91 ± 0.01	16.17 ± 0.01	16.19 ± 0.01	16.19 ± 0.02
18/05/2013	245 6431.21	21.71		17.36 ± 0.01	16.32 ± 0.01	16.17 ± 0.01	16.03 ± 0.01
20/05/2013	245 6433.21	23.71	17.77 ± 0.17	17.56 ± 0.02	16.40 ± 0.01	16.10 ± 0.02	16.01 ± 0.01
21/05/2013	245 6434.26	24.76		17.85 ± 0.02	16.55 ± 0.02	16.34 ± 0.05	16.16 ± 0.08
27/05/2013	245 6440.18	30.68		18.25 ± 0.02	16.80 ± 0.02	16.44 ± 0.01	16.08 ± 0.02
28/05/2013	245 6441.23	31.73			16.87 ± 0.01	16.53 ± 0.02	16.09 ± 0.01
29/05/2013	245 6442.22	32.72	18.37 ± 0.05	18.34 ± 0.01	16.89 ± 0.01	16.52 ± 0.01	16.06 ± 0.02
30/05/2013	245 6443.23	33.73	18.42 ± 0.03	18.40 ± 0.01	16.96 ± 0.01	16.57 ± 0.01	16.14 ± 0.02
31/05/2013	245 6444.19	34.69	18.40 ± 0.04	18.43 ± 0.01	16.97 ± 0.01	16.66 ± 0.01	16.28 ± 0.02
04/06/2013	245 6448.21	38.71	18.69 ± 0.04	18.66 ± 0.01	17.30 ± 0.01	16.89 ± 0.02	16.47 ± 0.02
13/06/2013	245 6457.23	47.73		18.72 ± 0.03	17.57 ± 0.05	17.35 ± 0.02	16.94 ± 0.03
04/07/2013	245 6478.17	68.67	18.98 ± 0.05	19.17 ± 0.02	18.19 ± 0.01	18.13 ± 0.02	18.15 ± 0.03
				PSN J0910 + 5003			
10/11/2015	245 7337.46	−9.54		17.71 ± 0.04	17.65 ± 0.03	17.54 ± 0.02	17.55 ± 0.02
17/11/2015	245 7344.38	−2.62	16.70 ± 0.11	17.16 ± 0.03	17.02 ± 0.02	16.89 ± 0.02	16.93 ± 0.02
19/11/2015	245 7346.49	−0.51		17.15 ± 0.05	16.99 ± 0.04	16.82 ± 0.06	16.94 ± 0.03
20/11/2015	245 7347.42	0.42		17.12 ± 0.03	16.95 ± 0.02	16.79 ± 0.02	16.97 ± 0.02
22/11/2015	245 7349.45	2.45	16.69 ± 0.04	17.18 ± 0.07	16.92 ± 0.03	16.71 ± 0.02	16.80 ± 0.05
27/11/2015	245 7354.44	7.44	17.07 ± 0.17	17.32 ± 0.04	16.91 ± 0.04	16.73 ± 0.04	16.89 ± 0.04
28/11/2015	245 7355.42	8.42		17.49 ± 0.08	16.95 ± 0.03	16.79 ± 0.10	16.80 ± 0.04
01/12/2015	245 7358.46	11.46		17.57 ± 0.04	17.03 ± 0.03	16.80 ± 0.02	16.91 ± 0.04
09/12/2015	245 7366.39	19.39		18.13 ± 0.03	17.31 ± 0.02	17.06 ± 0.02	16.97 ± 0.04
20/12/2015	245 7377.52	30.52		19.12 ± 0.11	17.75 ± 0.02	17.32 ± 0.02	17.02 ± 0.06
23/12/2015	245 7380.43	33.43		19.17 ± 0.12	17.87 ± 0.03	17.35 ± 0.03	16.98 ± 0.02
19/01/2016	245 7407.50	60.50			18.64 ± 0.03	18.28 ± 0.03	17.86 ± 0.05
25/01/2016	245 7413.27	66.27			18.80 ± 0.04	18.30 ± 0.04	17.96 ± 0.04
20/02/2016	245 7439.21	92.21				18.98 ± 0.06	18.40 ± 0.06
13/03/2016	245 7461.22	114.22		20.39 ± 0.10	19.71 ± 0.04	19.53 ± 0.05	18.93 ± 0.06
				ASASSN-16ex			
07/05/2016	245 7516.38	−6.87	16.41 ± 0.02	17.07 ± 0.02	17.03 ± 0.01	17.01 ± 0.01	17.16 ± 0.03
12/05/2016	245 7521.15	−2.10	16.22 ± 0.05	16.86 ± 0.01	16.81 ± 0.01	16.79 ± 0.02	16.92 ± 0.04
14/05/2016	245 7523.25	0.00	16.26 ± 0.03	16.84 ± 0.01	16.78 ± 0.02	16.78 ± 0.01	16.95 ± 0.03
16/05/2016	245 7525.28	2.03	16.28 ± 0.03	16.85 ± 0.02	16.78 ± 0.01	16.78 ± 0.02	16.95 ± 0.04
21/05/2016	245 7530.25	7.00	16.59 ± 0.05	17.04 ± 0.03	16.89 ± 0.03	16.90 ± 0.02	17.12 ± 0.04
03/06/2016	245 7543.36	20.11		17.93 ± 0.01	17.33 ± 0.01	17.21 ± 0.01	17.27 ± 0.02
10/06/2016	245 7550.42	27.17		18.46 ± 0.01	17.59 ± 0.02	17.30 ± 0.01	17.24 ± 0.02
18/06/2016	245 7558.31	35.06	18.89 ± 0.05	19.04 ± 0.03	17.95 ± 0.02	17.58 ± 0.04	17.40 ± 0.02
21/06/2016	245 7561.25	38.00	19.07 ± 0.08	19.14 ± 0.03	18.06 ± 0.02	17.65 ± 0.02	17.45 ± 0.02
26/06/2016	245 7566.37	43.12		19.33 ± 0.02	18.26 ± 0.01	17.85 ± 0.02	17.55 ± 0.02
06/07/2016	245 7576.17	52.92		19.47 ± 0.02	18.46 ± 0.01	18.20 ± 0.03	17.94 ± 0.04
10/07/2016	245 7580.16	56.91				18.36 ± 0.02	
31/07/2016	245 7601.13	77.88			19.04 ± 0.01	18.87 ± 0.02	18.73 ± 0.02
14/08/2016	245 7615.26	92.01		20.01 ± 0.04	19.28 ± 0.02	19.12 ± 0.02	18.99 ± 0.04
17/09/2016	245 7649.17	125.92		20.48 ± 0.10	19.96 ± 0.04	19.88 ± 0.08	19.89 ± 0.12

Note. [a] In days with respect to the epoch of the *B*-band maximum. All magnitudes are in the Vega system.

SNe Ia: SN 2003du ($\Delta m_{15}(B)$ = 1.04; Anupama et al. 2005), SN 2005cf ($\Delta m_{15}(B)$ = 1.11; Pastorello et al. 2007), SN 2011fe ($\Delta m_{15}(B)$ = 1.07; Brown et al. 2012; Richmond & Smith 2012; Vinkó et al. 2012), the luminous SN 1991T ($\Delta m_{15}(B)$ = 0.95; Lira et al. 1998), and 09dc-like SNe Ia: SN 2006gz (Hicken et al. 2007), SN 2007if (Scalzo et al. 2010), SN 2009dc (Taubenberger et al. 2011), ASASSN-15pz (Chen et al. 2019), SN 2012dn ($\Delta m_{15}(B)$ = 0.92; Chakradhari et al. 2014), and SN 2011aa ($\Delta m_{15}(B)$ = 0.59; Dutta et al. 2022). All the light curves are shifted to match their peak brightness and the epoch of the *B*-band maximum.

The comparison shows that SN 2013bz closely follows the light curves of normal type Ia SNe 2003du/05cf/11fe in the *BVRI* bands. The trough between the *I*-band primary and secondary maxima, the strength of the *I*-band secondary maximum, and the shoulder in the *R* band also match those of normal SNe Ia (refer to Fig. 6 for a zoomed view). Though the decline-rate parameter, $\Delta m_{15}(B)$, is lower than that of a typical SN Ia, SN 2013bz appears to be a perfectly normal Type Ia event.

On the other hand, *BVRI* light curves of PSN J0910 + 5003 and ASASSN-16ex are broad and closely follow 09dc-like events.

Table 3. UV–optical photometry of ASASSN-16ex with *Swift* UVOT.

JD	Phase[a]	*uvw*2	*uvm*2	*uvw*1	*u*	*b*	*v*
245 7514.46	−8.79	18.43 ± 0.18	18.04 ± 0.12	17.12 ± 0.10	16.28 ± 0.06	17.24 ± 0.08	17.32 ± 0.18
245 7517.70	−5.55	18.05 ± 0.15	17.71 ± 0.11	17.02 ± 0.09	16.14 ± 0.07	17.01 ± 0.08	16.90 ± 0.14
245 7522.75	−0.50	18.21 ± 0.17	18.09 ± 0.15	17.06 ± 0.10	16.10 ± 0.07	16.94 ± 0.08	16.78 ± 0.13
245 7530.21	6.96	18.94 ± 0.21	18.71 ± 0.19	18.05 ± 0.16	16.54 ± 0.07	16.98 ± 0.07	16.76 ± 0.11
245 7532.67	9.42	19.85 ± 0.78	19.36 ± 0.67	18.19 ± 0.26	16.83 ± 0.14	17.06 ± 0.12	17.02 ± 0.23
245 7537.52	14.27	19.75 ± 0.50	19.86 ± 0.54	18.94 ± 0.35	17.27 ± 0.13	17.41 ± 0.10	17.35 ± 0.22
245 7539.32	16.07	20.01 ± 0.55	19.91 ± 0.45	18.92 ± 0.29	17.73 ± 0.17	17.50 ± 0.11	17.20 ± 0.16
245 7541.85	18.60	20.28 ± 1.23	19.94 ± 0.51		18.01 ± 0.33	17.60 ± 0.16	17.19 ± 0.27
245 7544.50	21.25	20.16 ± 0.71	19.88 ± 0.50	19.17 ± 0.44	18.27 ± 0.33	17.80 ± 0.14	17.40 ± 0.26
245 7547.84	24.59			19.15 ± 0.24	18.44 ± 0.15	18.19 ± 0.14	17.74 ± 0.56
245 7551.21	27.96			19.33 ± 0.18	18.72 ± 0.12	18.56 ± 0.13	17.66 ± 0.14
245 7553.54	30.29			19.49 ± 0.31	18.77 ± 0.20	18.86 ± 0.24	17.79 ± 0.19
245 7557.45	34.20			19.82 ± 0.49	18.92 ± 0.29	19.00 ± 0.30	18.02 ± 0.28
245 7565.88	42.63			19.91 ± 0.43	19.42 ± 0.35	19.36 ± 0.29	18.28 ± 0.36
245 7572.28	49.03			20.19 ± 0.35	19.68 ± 0.25	19.34 ± 0.18	

Note. [a] In days with respect to the epoch of the *B*-band maximum. All magnitudes are in the Vega system.

Table 4. Log of spectroscopic observations of SN 2013bz, PSN J0910 + 5003, and ASASSN-16ex.

Date	JD[a]	Phase[b]	Range (Å)
	SN 2013bz		
30/04/2013	6413.30	3.80	3500–7000
02/05/2013	6415.16	5.66	3500–7000; 5200–9100
03/05/2013	6416.18	6.68	3500–7000; 5200–9100
06/05/2013	6419.26	9.76	3500–7000
09/05/2013	6422.19	12.69	3500–7000; 5200–9100
14/05/2013	6427.14	17.64	3500–7000; 5200–9100
20/05/2013	6433.25	23.75	3500–7000; 5200–9100
21/05/2013	6434.34	24.84	3500–7000
27/05/2013	6440.22	30.72	3500–7000; 5200–9100
29/05/2013	6442.24	32.74	3500–7000; 5200–9100
31/05/2013	6444.22	34.72	3500–7000; 5200–9100
	PSN J0910 + 5003		
17/11/2015	7344.42	−2.58	3500–7000; 5200–9100
20/11/2015	7347.44	0.44	3500–7000; 5200–9100
27/11/2015	7354.39	7.39	3500–7000; 5200–9100
28/11/2015	7355.36	8.36	3500–7000; 5200–9100
09/12/2015	7366.41	19.41	3500–7000; 5200–9100
20/12/2015	7377.45	30.45	3500–7000; 5200–9100
19/01/2016	7407.41	60.41	3500–7000; 5200–9100
22/01/2016	7410.24	63.24	3500–7000; 5200–9100
	ASASSN-16ex		
06/05/2016	7515.42	−7.83	3500–7000
08/05/2016	7517.41	−5.84	3500–7000; 5200–9100
13/05/2016	7522.17	−1.08	3500–7000; 5200–9100
14/05/2016	7523.16	−0.09	3500–7000; 5200–9100
21/05/2016	7530.27	7.02	3500–7000; 5200–9100
11/06/2016	7551.18	27.93	3500–7000
19/06/2016	7559.35	36.10	3500–7000; 5200–9100
26/06/2016	7566.30	43.05	3500–7000

Note. [a] 245 0000 + [b] In days from the *B*-band maximum.

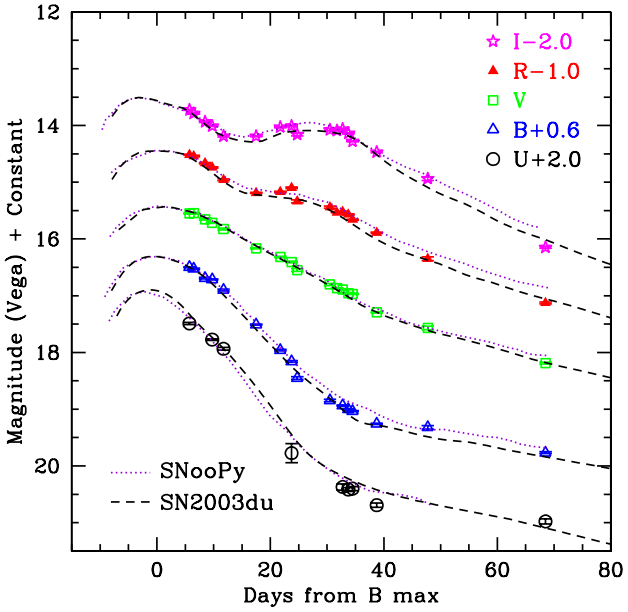

Figure 2. *UBVRI* light curves of SN 2013bz. The light curves are shifted vertically by the amount indicated in the legend. The phase is measured in days from the *B*-band maximum. The dotted lines represent the template light curves obtained using the SNooPy code. The dashed lines represent the light curves of the normal Type Ia SN 2003du.

Similarly to 09dc-like SNe, *I* band light curves of PSN J0910+5003 and ASASSN-16ex appear flat during the early post-maximum phase (until ∼ 40 d); in the later phase they also follow 09dc-like SNe. An enhanced fading is seen in the light curves of 09dc-like SNe in the nebular phase. In some events, e.g. SN 2012dn, ASASSN-15pz, and LSQ14fmg, it was observed quite early (1–3 months from the maximum phase). This is not observed in PSN J0910 + 5003 and ASASSN-16ex until our last observations (∼ 126 d: refer to Fig. 6, right panel).

The decline rates of ASASSN-16ex and PSN J0910 + 5003 in the *BVRI* bands during 50–100 d are estimated by a linear fit and listed in Table 6. The late-phase decline of ASASSN-16ex and PSN J0910 + 5003 light curves is comparable to that of SNe 2007if/09dc.

In Fig. 7, the *UV* light curves of ASASSN-16ex in *uvu*, *uvw*2, *uvm*2, and *uvw*1 bands are compared with those of normal and 09dc-like SNe Ia. It is clear that the light curves of ASASSN-16ex in all the *UV* bands are distinct from normal SNe 2005cf/11fe and closely follow those of 09dc-like SNe. Similarly to 09dc-like SNe, the *UV* light curves of ASASSN-16ex in *uvw*2, *uvm*2, and *uvw*1 reached maximum light a few days before the normal SNe 2005cf/11fe. Also,

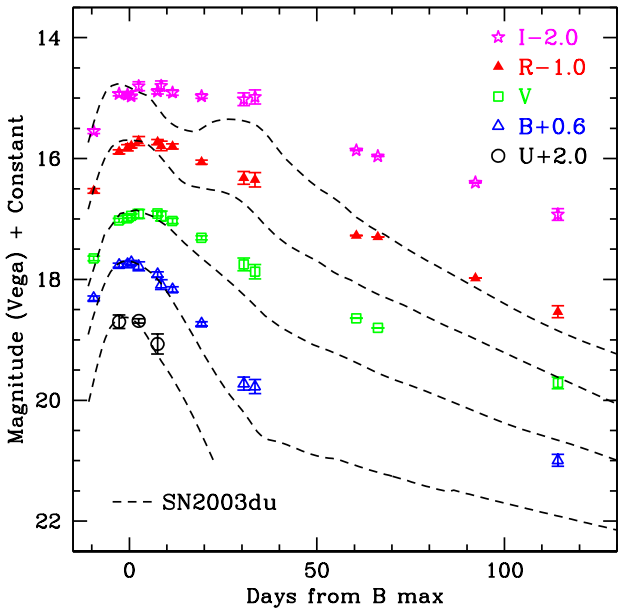

Figure 3. *UBVRI* light curves of PSN J0910 + 5003. The light curves are shifted vertically by the amount indicated in the legend. The dashed lines represent the light curves of the normal Type Ia SN 2003du.

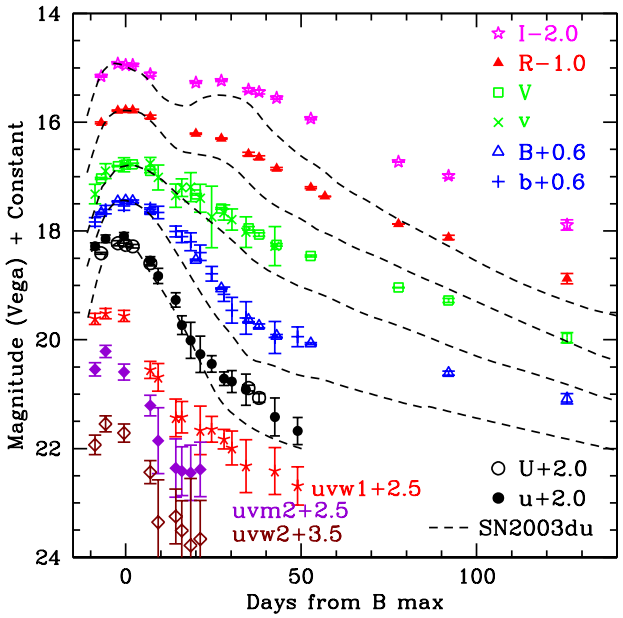

Figure 4. *UBVRI* and *Swift* UVOT light curves of ASASSN-16ex. The light curves are shifted vertically by the amount indicated in the legend. The dashed lines represent the light curves of the normal Type Ia SN 2003du.

the *UV* light curves of ASASSN-16ex and 09dc-like SNe are broader than those of normal events.

The reddening-corrected (refer to Section 4.1) $(uvw1 - v)$, $(U - B)$, $(B - V)$, $(V - R)$, and $(R - I)$ colour curves of SN 2013bz, PSN J0910 + 5003, and ASASSN-16ex are plotted in Fig. 8. Colour curves of well-studied SNe Ia (used in the light-curve comparison) are also plotted in Fig. 8. They are corrected for reddening, as mentioned in their respective references.

Table 5. Timing of maximum light in *UVRI* bands (in days) with respect to the *B*-band maximum.

Object	*U*	*V*	*R*	*I*	Ref.[a]
SN 2013bz	−2.0	+ 0.2	+ 1.0	−3.0	1
PSN J0910 + 5003	–	+ 5.0	+ 4.0	+ 6.0	1
ASASSN-16ex	−1.5	+ 1.5	0	−1.8	1
SN 2006gz	−3.0	+ 2.0	+ 6.0	+ 6.0	2
SN 2009dc	−2.0	0	+ 1.0	+ 2	3
SN 2012dn	−2.5	+ 1.6	+ 2.6	+ 3	4
ASASSN-15pz	–	∼0	+ 1	+ 0.4	5
ASASSN-15hy	−6.0	+ 3.0	+ 5.5	+ 7.3	6
LSQ14fmg	–	−1.0	+ 1	+ 1	7
SN 2020esm	−4.0	∼0	+ 3.5	+ 5	8
SN 2020hvf	−4.0	+ 1.0	+ 1.8	+ 2.7	9
SN 2011aa	−0.3	+ 3.8	+ 4.5	+ 7.1	10
SN 2003du	−1.3	+ 1.0	+ 0.3	−1.9	11
SN 2005cf	−1.6	+ 1.3	+ 0.6	−2.0	12
SN 2011fe	−1.4	+ 1.0	+ 0.6	−2.9	13, 14
SN 1991T	−1.7	+ 2.6	+ 1.4	−0.4	15

Notes. [a]1. This work, 2. Hicken et al. (2007), 3. Taubenberger et al. (2011), 4. Chakradhari et al. (2014), 5. Chen et al. (2019), 6. Lu et al. (2021), 7. Hsiao et al. (2020), 8. Dimitriadis et al. (2022), 9. Jiang et al. (2021), 10. Dutta et al. (2022), 11. Anupama, Sahu & Jose (2005), 12. Pastorello et al. (2007), 13. Richmond & Smith (2012), 14. Pereira et al. (2013), 15. Lira et al. (1998).

The $(uvw1 - v)$ colour evolution of ASASSN-16ex is similar to that of 09dc-like SNe. The normal SNe 2005cf/11fe are redder in the early phase and evolve to blue, with the bluest value a few days before the *B*-band maximum. Their $(uvw1 - v)$ colour evolution makes a characteristic V-shape pattern (Milne et al. 2013; Brown et al. 2014b). However, ASASSN-16ex is bluer by ∼1 mag in the early phase and reddens monotonically, similar to other 09dc-like SNe. Milne et al. (2013) have divided normal SNe Ia into NUV-blue and NUV-red categories based on the (near-UV − optical) colour evolution. The shaded region in Fig. 8 (top panel) shows the colour evolution of normal SNe Ia (which includes NUV-blue and NUV-red objects: Milne et al. 2013; Brown et al. 2014b). With a significantly blue (near-UV − optical) colour, ASASSN-16ex and 09dc-like SNe Ia are clearly distinguishable from normal SNe Ia. This colour criterion can be used to separate 09dc-like objects from the SNe Ia sample with a precise host extinction estimate. The $(U - B)$ colour of SN 2013bz, PSN J0910 + 5003, and ASASSN-16ex is bluer relative to normal events.

The $(B - V)$ colour of SN 2013bz follows that of normal SNe Ia, while ASASSN-16ex follows the evolution of 09dc-like SNe 2006gz/09dc/ASASSN-15pz in the complete phase range. The 09dc-like SNe 2006gz/09dc/ASASSN-15pz have a bluer curve during 0 to +50 d, while normal SNe 2003du/05cf/11fe and 91T have a relatively red colour. PSN J0910 + 5003 appears to follow a redder path, similarly to normal SNe Ia.

The $(V - R)$ colour of ASASSN-16ex is similar to that of SN 2009dc up to ∼ 100 d; PSN J0910 + 5003 has a more gradual and redder colour evolution. The $(R - I)$ colour of ASASSN-16ex is a little bluer but similar to SN 2009dc, while PSN J0910 + 5003 has a colour similar to SN 2007if. Compared with normal events, the $(V - R)$ and $(R - I)$ colours of 09dc-like SNe show less evolution, i.e. red to blue change, because of their broad *RI* light curves. The scatter in the colours within the 09dc-like SNe group can be attributed to their differing *RI* light curves. The $(V - R)$ and $(R - I)$ colours of SN 2013bz are similar to those of normal events.

Table 6. Photometric parameters of SN 2013bz, PSN J0910 + 5003, and ASASSN-16ex.

Band	JD (max)	$m_\lambda^{\max}$	$M_\lambda^{\max}$	$\Delta m_{15}(\lambda)$	Decline rate[a]
		SN 2013bz			(35–70 d)
U	245 6407.2 ± 0.8	14.93 ± 0.06	−20.53 ± 0.20	1.21 ± 0.06	1.52
B	245 6409.5 ± 0.8	15.71 ± 0.04	−19.61 ± 0.20	0.91 ± 0.04	2.07
V	245 6409.7 ± 0.8	15.42 ± 0.04	−19.70 ± 0.20	0.57 ± 0.04	3.48
R	245 6410.2 ± 0.8	15.44 ± 0.07	−19.53 ± 0.20	0.66 ± 0.07	4.38
I	245 6406.3 ± 0.8	15.51 ± 0.09	−19.30 ± 0.20	0.59 ± 0.09	5.62
		PSN J0910 + 5003			(50–100 d)
B	245 7347.0 ± 0.6	17.13 ± 0.05	−19.44 ± 0.20	0.69 ± 0.05	1.51
V	245 7352.0 ± 0.8	16.90 ± 0.04	−19.48 ± 0.20	0.44 ± 0.04	1.96
R	245 7351.2 ± 0.8	16.70 ± 0.05	−19.54 ± 0.20	0.35 ± 0.04	2.43
I	245 7353.0 ± 0.9	16.80 ± 0.05	−19.29 ± 0.20	0.18 ± 0.05	1.95
		ASASSN-16ex			(50–100 d)
*uvw*2	245 7517.7 ± 0.6	18.05 ± 0.15	−18.80 ± 0.30	1.27 ± 0.15	–
*uvm*2	245 7517.7 ± 0.6	17.71 ± 0.11	−19.36 ± 0.30	1.51 ± 0.11	–
*uvw*1	245 7517.7 ± 0.6	17.02 ± 0.09	−19.75 ± 0.30	1.26 ± 0.09	–
U	245 7521.7 ± 0.7	16.23 ± 0.05	−20.47 ± 0.20	0.91 ± 0.05	–
B	245 7523.2 ± 0.5	16.84 ± 0.03	−19.78 ± 0.20	0.72 ± 0.03	2.14
V	245 7524.7 ± 0.5	16.77 ± 0.03	−19.71 ± 0.20	0.43 ± 0.03	2.14
R	245 7523.2 ± 0.6	16.78 ± 0.03	−19.62 ± 0.20	0.35 ± 0.03	2.54
I	245 7521.5 ± 0.6	16.94 ± 0.04	−19.35 ± 0.20	0.31 ± 0.04	2.97

Note. [a] In units of mag (100 d)$^{-1}$.

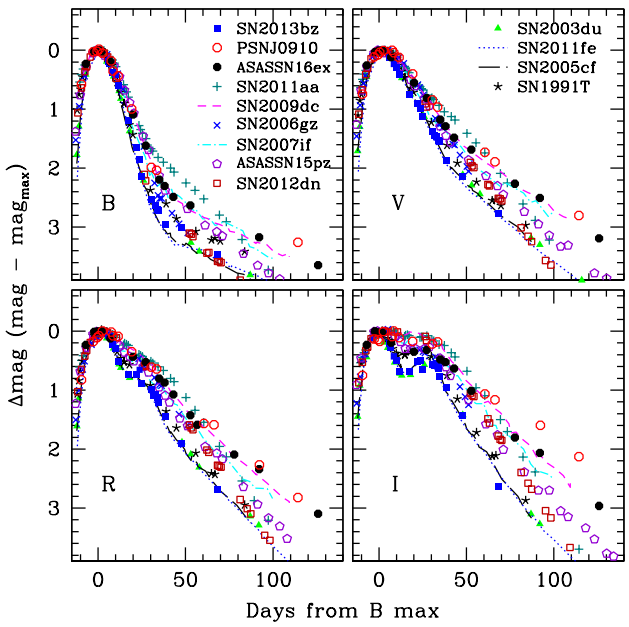

Figure 5. *BVRI* light curves of SN 2013bz, PSN J0910 + 5003, and ASASSN-16ex are compared with those of some other well-studied SNe Ia. The light curves are shifted to match their peak brightness and the epoch of the *B*-band maximum.

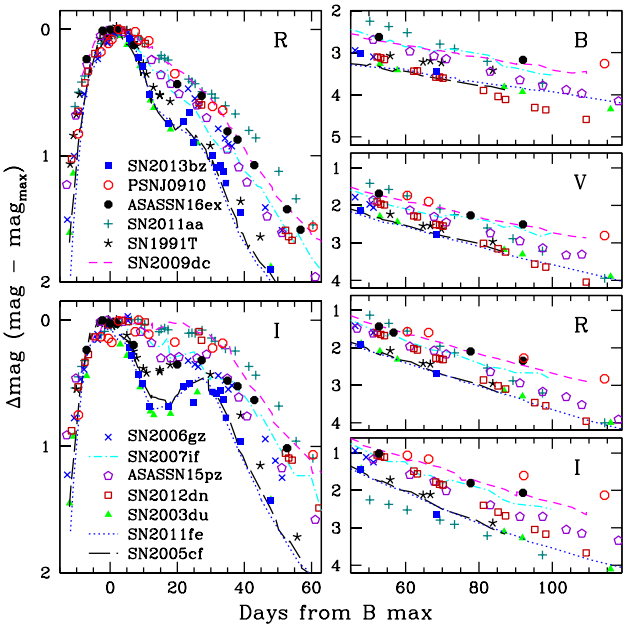

Figure 6. A zoomed view of the light-curve comparison. Left: *R*- and *I*-band light curves during the secondary maximum. Right: *BVRI* light curves during the late phase.

4 ABSOLUTE LIGHT CURVES AND BOLOMETRIC LUMINOSITY

4.1 Reddening estimate

The Galactic reddening for SN 2013bz is $E(B-V)_{\rm Gal}$ = 0.04 ± 0.002 mag (Schlafly & Finkbeiner 2011). Empirical relations (Phillips et al. 1999; Altavilla et al. 2004; Reindl et al. 2005; Wang et al. 2006; Folatelli et al. 2010) suggest a large total reddening, $E(B-V)_{\rm total}$ = 0.30–0.40 mag. The SNooPy fit suggests a reddening of $E(B-V)_{\rm total}$ = 0.21 ± 0.06 mag. A strong Na I D feature is seen in the rest frame of the host galaxy in the spectra of SN 2013bz, with an average equivalent width (EW) of 1.9 ± 0.2 Å. The Milky Way component of the Na I D feature is not detectable. The measured EW (Na I D) translates into $E(B-V)_{\rm host}$ = 0.29 ± 0.03 mag (Turatto, Benetti & Cappellaro 2003), close to the value obtained using other empirical relations. We found that the observed $(B-V)$ colour curve of SN 2013bz matches well with that of normal SNe Ia (refer to Fig. 8) when it is dereddened by $E(B-V)_{\rm total}$ = 0.19 ± 0.04 mag.

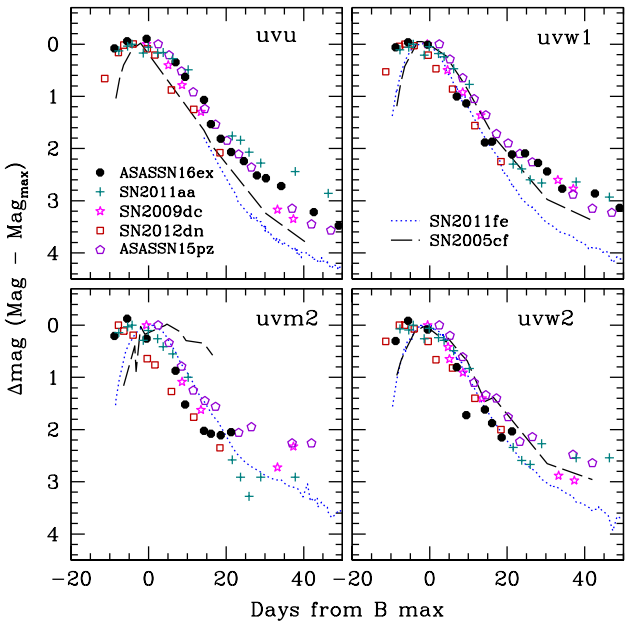

Figure 7. *UV* light curves of ASASSN-16ex are compared with those of some well-studied SNe Ia. The light curves are shifted to match their peak brightness and the epoch of the *B*-band maximum.

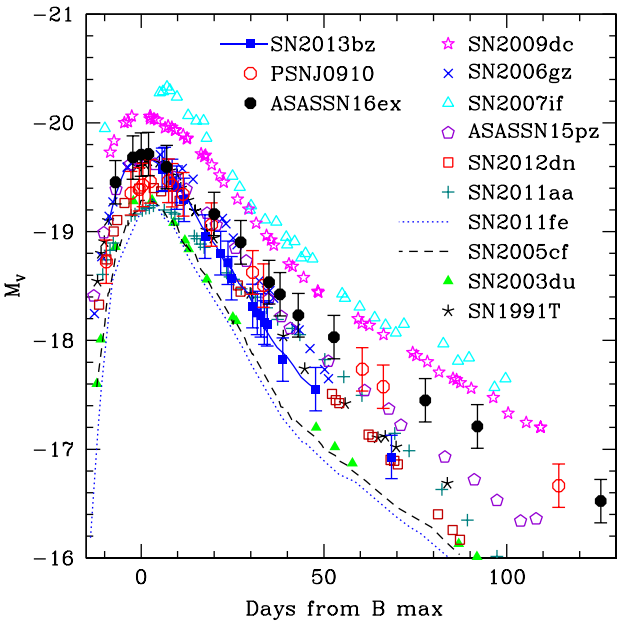

Figure 9. Absolute *V*-band light curves of SN 2013bz, PSN J0910 + 5003, and ASASSN-16ex are compared with those of other well-studied SNe Ia.

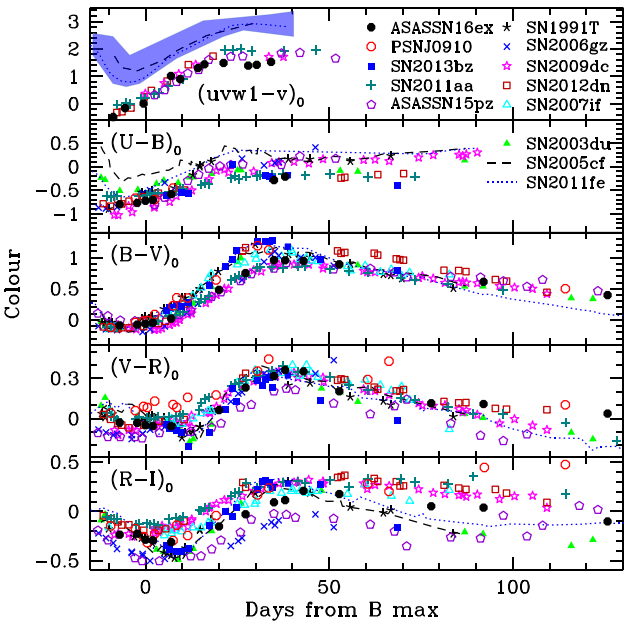

Figure 8. The ($uvw1 - v$), ($U - B$), ($B - V$), ($V - R$), and ($R - I$) colour curves of SN 2013bz, PSN J0910 + 5003, and ASASSN-16ex are compared with those of other well-studied SNe Ia. The shaded region in the top panel shows the ($uvw1 - v$) colour evolution of normal (NUV-blue + NUV-red: Milne et al. 2013; Brown et al. 2014b) SNe Ia.

This estimate is close to the value suggested by the SNooPy fit and is used for further analysis.

The Galactic reddening for PSN J0910 + 5003 is $E(B - V)_{\rm Gal}$ = 0.02 ± 0.001 mag (Schlafly & Finkbeiner 2011). The empirical relations using photometry suggest $E(B - V)_{\rm total} > 0.25$ mag. The Na I D features are not detected in the spectra of PSN J0910 + 5003. The observed ($B - V$) colour curve of PSN J0910 + 5003 matches well with those of other well-studied SNe Ia (refer to Fig. 8) after correcting it by $E(B - V)_{\rm total} = 0.18 \pm 0.05$ mag, which we use in our analysis.

The Galactic reddening for ASASSN-16ex is $E(B - V)_{\rm Gal}$ = 0.03 ± 0.001 mag (Schlafly & Finkbeiner 2011). The empirical relations suggest $E(B - V)_{\rm total} \sim 0.11$–$0.18$ mag. No feature of Na I D is detected in the spectra of ASASSN-16ex. It was shown (refer to Section 3) that the photometric properties of ASASSN-16ex closely resemble those of 09dc-like SNe Ia. Chen et al. (2019) found that, among 09dc-like SNe, ASASSN-15pz suffered minimal reddening, and its colour evolution can be used to estimate the reddening of similar objects. The observed ($B - V$) colour curve of ASASSN-16ex matches well with those of ASASSN-15pz and other 09dc-like objects after a correction by $E(B - V)_{\rm total} = 0.12 \pm 0.04$ mag. Hence, we use this value of total reddening in further analysis.

4.2 Absolute magnitudes

The recession velocity corrected for the infall of the Local Group towards the Virgo cluster is 5 807 ± 45 km s^{-1} for PGC 170248, and for UGC 4812 it is 10 503 ± 31 km s^{-1} (Mould et al. 2000; source NED). With H_0 = 72 ± 5 km s^{-1} Mpc^{-1} (Freedman et al. 2001), the distances of SN 2013bz and PSN J0910+5003 are calculated as 80.65 ± 5.6 Mpc (μ = 34.53 ± 0.20 mag) and 145.88 ± 10 Mpc (μ = 35.82 ± 0.20 mag), respectively. For SDSS J171023.63 + 262350.3 (host of ASASSN-16ex), using z = 0.04 (Foley et al. 2018), we derived a distance of 166.67 ± 12 Mpc (μ = 36.11 ± 0.20 mag).

Using the estimated distances, reddening values, and Cardelli, Clayton & Mathis (1989) extinction law with $R_V = 3.1$, the peak absolute magnitudes of SN 2013bz, PSN J0910 + 5003, and ASASSN-16ex in different bands are estimated and listed in Table 6. The absolute *V*-band light curves of these SNe are displayed in Fig. 9 and compared with those of other well-studied SNe Ia. SN 2013bz and ASASSN-16ex have luminosities comparable to SNe 2006gz/91T

and ASASSN-15pz. The light curve of SN 2013bz is similar to that of SN 1991T. With a constant difference of ~ 0.4 mag, the absolute *V*-band light curve of ASASSN-16ex runs almost parallel to that of SN 2009dc. The light curve of PSN J0910+5003 is fainter than those of 09dc-like objects but brighter than those of normal SNe 2003du/05cf/11fe. At maximum, PSN J0910 + 5003 is fainter than ASASSN-16ex. However, during the late phase they show similar light-curve evolution.

4.3 Bolometric light curve

The quasi-bolometric luminosities of SN 2013bz, PSN J0910 + 5003, and ASASSN-16ex were derived using the observed *UBVRI* magnitudes in Table 2. The *UBVRI* magnitudes were dereddened with the reddening values estimated in Section 4.1 and converted to monochromatic fluxes using zero points from Bessell, Castelli & Plez (1998). The derived fluxes on each night were integrated over the observed wavelength range to obtain the total flux in the optical bands. The integrated flux is converted to quasi-bolometric luminosity using the distances derived in Section 4.2.

The peak quasi-bolometric luminosity for SN 2013bz obtained by integration of optical fluxes is $\log L_{\rm bol}^{\rm max} = 43.30\,{\rm erg\,s^{-1}}$. Adding 20 per cent flux to account for the contribution from the missing bands (Wang et al. 2009a) results in $\log L_{\rm bol}^{\rm max} = 43.38 \pm 0.07\,{\rm erg\,s^{-1}}$.

The maximum quasi-bolometric luminosity for ASASSN-16ex is obtained as $\log L_{\rm bol}^{\rm max} = 43.29\,{\rm erg\,s^{-1}}$ using optical observations. We used *Swift* UVOT data of ASASSN-16ex to estimate the contributions from UV bands. The UV magnitudes were dereddened following Brown et al. (2010) and converted to monochromatic flux using the zero points from Poole et al. (2008). With the UV contribution, the peak bolometric luminosity of ASASSN-16ex becomes $\log L_{\rm bol}^{\rm max} = 43.39\,{\rm erg\,s^{-1}}$. The UV contribution to the bolometric luminosity is found as $\sim$ 29, 22, and 13 per cent at -7 d, maximum, and + 20 d, respectively. 09dc-like SNe Ia are found to be UV-bright (Chakradhari et al. 2014; Brown et al. 2014b; Chen et al. 2019; Dimitriadis et al. 2022), and ASASSN-16ex follows a similar trend. After adding 5 per cent contribution from NIR bands (Wang et al. 2009a; Scalzo et al. 2010; Yamanaka et al. 2016), the peak bolometric luminosity of ASASSN-16ex is estimated as $\log L_{\rm bol}^{\rm max} = 43.40 \pm 0.06\,{\rm erg\,s^{-1}}$.

The peak quasi-bolometric luminosity for PSN J0910 + 5003 is derived as $\log L_{\rm bol}^{\rm max} = 43.17\,{\rm erg\,s^{-1}}$ by integrating the optical data points. For 09dc-like objects, close to the maximum, the UV band contributes ~ 20 per cent (Chakradhari et al. 2014) to the bolometric flux. We found a similar UV contribution in ASASSN-16ex. On adding 20 per cent UV and 5 per cent NIR contributions, the peak bolometric luminosity of PSN J0910 + 5003 is obtained as $\log L_{\rm bol}^{\rm max} = 43.26 \pm 0.07\,{\rm erg\,s^{-1}}$.

The quasi-bolometric light curves of SN 2013bz, PSN J0910 + 5003, and ASASSN-16ex are plotted in Fig. 10 and compared with those of other well-studied SNe Ia. The peak quasi-bolometric luminosities of SN 2013bz, PSN J0910 + 5003, and ASASSN-16ex are lower than those of 09dc-like SNe 2006gz/07if/09dc/ASASSN-15pz and brighter than those of normal SNe Ia.

4.4 Mass of nickel synthesized

Type Ia SNe are powered by the radioactive decay of ^{56}Ni to ^{56}Co and subsequently to ^{56}Fe. The peak bolometric luminosity can be used to estimate the mass of ^{56}Ni synthesized in the explosion of SNe Ia.

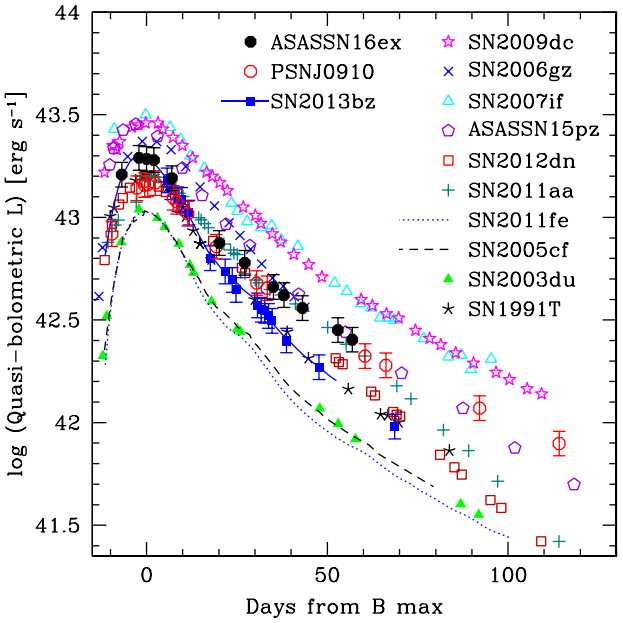

Figure 10. Quasi-bolometric light curves of SN 2013bz, PSN J0910 + 5003, and ASASSN-16ex are plotted, along with those of other well-studied SNe Ia.

The mass of ^{56}Ni synthesized in the explosions of SN 2013bz, PSN J0910 + 5003, and ASASSN-16ex is estimated using Arnett's rule (Arnett 1982). This rule states that the peak bolometric luminosity of a type Ia SN is proportional to the instantaneous energy release rate from radioactive decay. This can be written as

$$\mathrm{M_{Ni}} = \frac{L_{\rm bol}^{\rm max}}{\alpha \dot{S}(t_{\rm R})},$$

where $\mathrm{M_{Ni}}$ is the mass of ^{56}Ni, α is the ratio of bolometric to radioactive luminosities (near unity), and $\dot{S}(t_{\rm R})$ is the radioactivity luminosity per unit nickel mass evaluated for the rise time $t_{\rm R}$. From Nadyozhin (1994), $\dot{S}(t_R)$ can be written as

$$\dot{S}(t_{\rm R}) = \left(6.45\,{\rm e}^{-(t_{\rm R}/8.8{\rm d})} + 1.45\,{\rm e}^{-(t_{\rm R}/111.3{\rm d})}\right) \times 10^{43}\,{\rm erg\,s^{-1}M_{\odot}^{-1}},$$

where 8.8 and 111.3 d are the e-folding lifetimes (τ) of ^{56}Ni and ^{56}Co, respectively.

With the lack of early observations, it is difficult to constrain the explosion epochs and rise times of these events. This limits an accurate determination of the mass of ^{56}Ni. The rise time ($t_{\rm R}$) for normal SNe Ia is found to be 17.4 d (Hayden et al. 2010), 18 d (Ganeshalingam, Li & Filippenko 2011), 18.9 d (Firth et al. 2015; Miller et al. 2020), and 19.1–19.6 d (Riess et al. 1999; Conley et al. 2006). Using $t_{\rm R} = 18 \pm 2$ d and $\alpha = 1.2 \pm 0.2$ (Branch 1992), the mass of ^{56}Ni synthesized in the explosion of SN 2013bz is estimated as $\mathrm{M_{Ni}} = 0.96 \pm 0.24\,\mathrm{M_{\odot}}$. 09dc-like SNe are found to have longer $t_{\rm R}$ $\sim$ 21–24 d (Scalzo et al. 2010; Silverman et al. 2011; Chen et al. 2019; Lu et al. 2021), with an average of $t_{\rm R} \sim 22 \pm 4$ d (Ashall et al. 2021). Using $t_{\rm R} = 22$ d and $\alpha = 1.2$, the mass of ^{56}Ni in PSN J0910 + 5003 and ASASSN-16ex is estimated as $\mathrm{M_{Ni}} = 0.89 \pm 0.24\,\mathrm{M_{\odot}}$ and $1.2 \pm 0.32\,\mathrm{M_{\odot}}$, respectively.

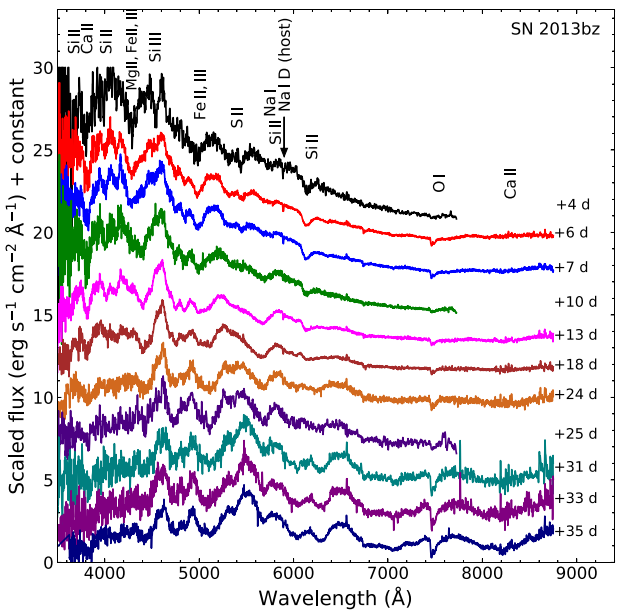

Figure 11. Spectral evolution of SN 2013bz from ∼ +4 to + 35 d.

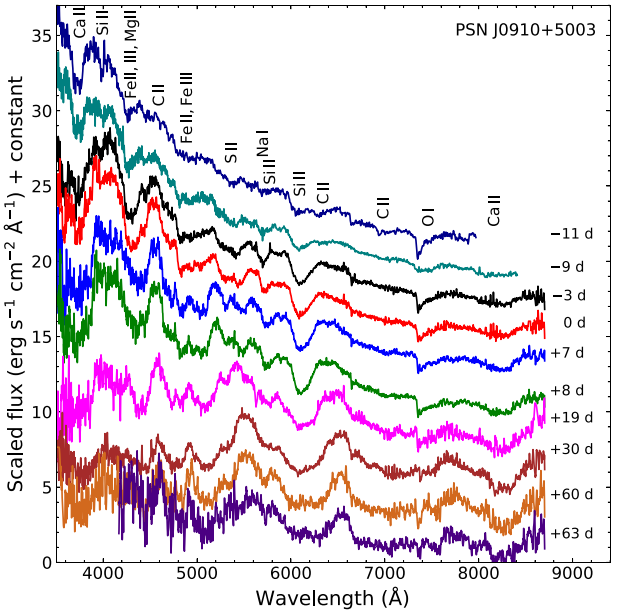

Figure 12. Spectral evolution of PSN J0910+5003 from ∼−11 to + 63 d.

5 SPECTRAL EVOLUTION

Spectral series were obtained for SN 2013bz, PSN J0910+5003, and ASASSN-16ex using HFOSC-HCT. In total, 11 spectra spanning +4 to +35 d for SN 2013bz, eight spectra from −3 to +63 d for PSN J0910+5003, and eight spectra from −8 to + 43 d for ASASSN-16ex were obtained.[4] The details of the spectroscopic observations are given in Table 4. The spectral evolution of SN 2013bz, PSN J0910 + 5003, and ASASSN-16ex is presented in Figs 11, 12, and 13, respectively. All the spectra are reddening- and redshift-corrected. Telluric lines are not removed.

Spectral features in the early phase of Type Ia SNe are mostly absorption lines of singly ionized IMEs such as O, Mg, Si, S, and Ca produced in the outer photospheric layers. As the ejecta expands, the photosphere moves into deeper layers, and lines from the inner layers are seen. During this, features from IMEs are replaced by IGEs, e.g. Fe, Co and Ni.

5.1 SN 2013bz

The early post-maximum spectra of SN 2013bz (+4, +6, and + 7 d) show the characteristic features of SNe Ia, mostly from IMEs marked in Fig. 11. At the bluer end, a deep absorption seen around 4000 Å is due to Ca II H&K lines. The next prominent and broad feature at around 4500 Å is due to a blend of Fe III λ4404, Mg II λ4481, and Fe II λ4555. Moving red-ward, a sharp absorption due to Si III λ4560 is seen in the first spectrum at +4 d, which has become weak in the following spectrum at + 6 d. Si III λ4560 is generally seen during the early hot photospheric phase. A broad blend is seen at ∼ 5000 Å due to Fe II λλ4924, 5018, Si II λ5051, Fe III λ5129, and Fe II λ5169. The W-shaped S II λλ5654, 5468 feature is also visible, with decreasing strength in subsequent spectra. Features on the red side of the spectrum, such as O I and Ca II NIR, are weak in SN 2013bz. A small narrow feature seen at ∼ 6000 Å is due to Na I D from the host galaxy.

In the spectra obtained at +10, +13, and + 18 d, most of the features due to IMEs such as W-shaped S II and Si II weakened/disappeared. The features due to IMEs are being replaced by Fe II lines. Development of emission peaks, such as at ∼ 4600 Å, can also be noticed. Strong absorption due to Na I from SN ejecta is visible at ∼ 5700 Å. The spectra after one month post-maximum are dominated by Fe II lines. The feature due to the Ca II NIR triplet looks stronger than earlier.

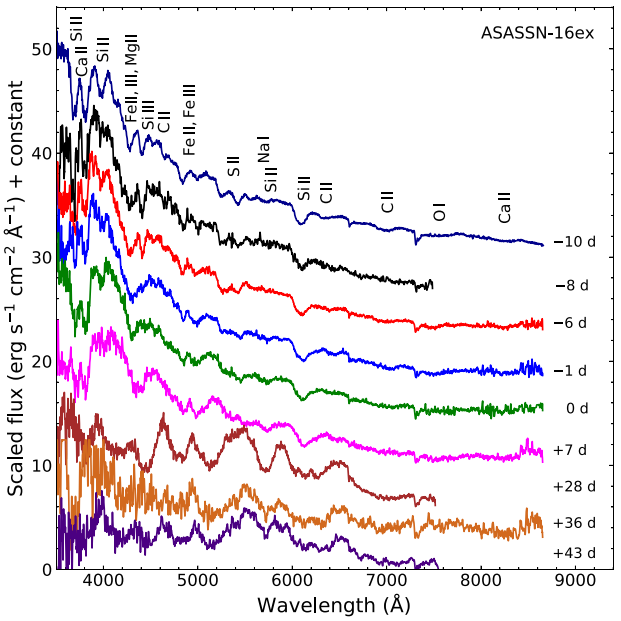

Figure 13. Spectral evolution of ASASSN-16ex from ∼−10 to + 43 d.

[4]Phase with respect to *B*-band maximum.

5.2 PSN J0910 + 5003

The spectral evolution of PSN J0910+5003 from −11 to + 63 d is shown in Fig. 12. The first two spectra at −11 and −9 d are taken from the Weizmann Interactive Supernova Data Repository (WISeREP: Tomasella et al. 2015; Stahl et al. 2020) and displayed to show the early evolution and spectral characteristics. The first spectrum at −11 d looks like a featureless continuum; most spectral lines are shallow/not yet fully developed. Strong C II λ6580 absorption can be seen in the red wing of Si II λ6355, which makes the absorption at ∼ 6200 Å very broad. This indicates the presence of unburned material in the ejecta, usually found in 09dc-like SNe Ia (Taubenberger et al. 2011; Chakradhari et al. 2014; Chen et al. 2019; Jiang et al. 2021; Lu et al. 2021; Dimitriadis et al. 2022; Srivastav et al. 2023).

In the spectrum at −9 d, the features from IMEs are strengthening. The carbon lines have almost disappeared; only a tiny suppression is seen in the red wing of Si II λ6355. By −3 d, the absorption features due to IMEs are fully developed and dominate the spectra till one week post-maximum. In contrast to SN 2013bz, features like Si II λ5972, O I, and Ca II NIR are stronger in PSN J0910+5003. The spectrum at + 19 d and subsequent spectra show the appearance of several emission peaks due to IGEs. Fe II lines have replaced the features from IMEs.

5.3 ASASSN-16ex

The spectral evolution of ASASSN-16ex from −10 to + 43 d is shown in Fig. 13. The first spectrum at −10 d is taken from WISeREP (Tomasella et al. 2016). Similarly to PSN J0910 + 5003, the signature of unburned C II is seen in this object. Compared with PSN J0910 + 5003, spectral features in ASASSN-16ex are well developed and sharp. The Si II λ5972, O I, and Ca II NIR features are weaker in ASASSN-16ex than PSN J0910 + 5003. Along with a weak Si II λ5972 line, a strong Si III λ4560 feature is present in the spectrum of ASASSN-16ex, suggesting a hot photosphere. In the spectrum at ∼ one month and in subsequent spectra, the features of IMEs are replaced by Fe II lines and the development of emission lines can be seen.

5.4 Spectral comparison

In Fig. 14 (top panel), the early spectra of PSN J0910 + 5003 (−11, −9 d) and ASASSN-16ex (−10 d) are compared with those of SN 1991T (Filippenko et al. 1992), SN 2006gz (Hicken et al. 2007), SN 2007if (Scalzo et al. 2010), SN 2009dc (Taubenberger et al. 2011), SN 2011fe (Parrent et al. 2012), SN 2011aa (Dutta et al. 2022), and ASASSN-15pz (Chen et al. 2019) at a similar epoch. Though the lines in PSN J0910+5003 are shallower, the spectra of both PSN J0910 + 5003 and ASASSN-16ex are similar to those of 09dc-like SNe. Strong C II features are seen in both events.

The spectral features of ASASSN-16ex are very similar to those of 2006gz/09dc/12dn. In the bluer region, well-separated sharp absorption due to Si II λ3858, Ca II H&K, Si II λ4130, and Si III λ4560 is identical in these events. Other features like W-shaped S II, Si II λ6355, and a shallower Si II λ5972 look similar in these objects. The spectral features in PSN J0910+5003 at −11 and −9 d are similar to those in SN 2007if and SN 2011aa. A comparison of spectra of PSN J0910 + 5003, ASASSN-16ex, and other SNe is made at the maximum phase in the bottom panel of Fig. 14. At this phase also, ASASSN-16ex closely resembles SN 2012dn/06gz. The spectrum of PSN J0910+5003 is similar to that of SN 2011aa. Absorption lines in PSN J0910 + 5003 appear broader and blended.

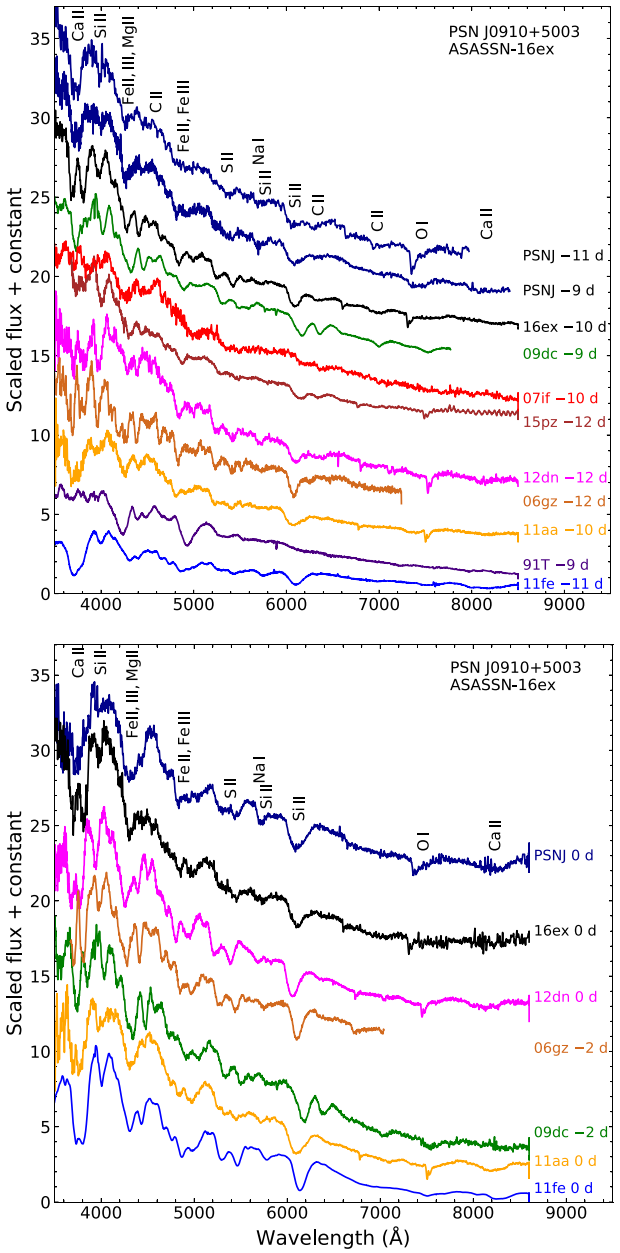

Figure 14. Spectra of PSN J0910 + 5003 and ASASSN-16ex at ∼− 10 d (top) and at maximum (bottom) are compared with other well-studied SNe Ia.

In Fig. 15, the spectrum of ASASSN-16ex ∼ four months after maximum light (taken from WISeREP: Stahl et al. 2020) is compared with those of SN 2011fe (Stahl et al. 2020), SN 2007if (Silverman et al. 2011), SN 2009dc (Taubenberger et al. 2011), ASASSN-15pz (Chen et al. 2019), SN 1991T (Silverman et al. 2012), and SN 1991bg (Turatto et al. 1996) at a similar epoch. A few months after the explosion, SN enters into a nebular phase, the ejecta becomes optically thin, and the inner part of the ejecta becomes visible. Forbidden emission lines of IGEs, i.e. Fe, Co, and Ni, characterize spectra of SNe Ia at this phase. Some prominent nebular features are marked in Fig. 15. Similarity in the spectral features between ASASSN-16ex and a normal SN Ia can be seen. However, there are certain noticeable differences also. The blending of lines in

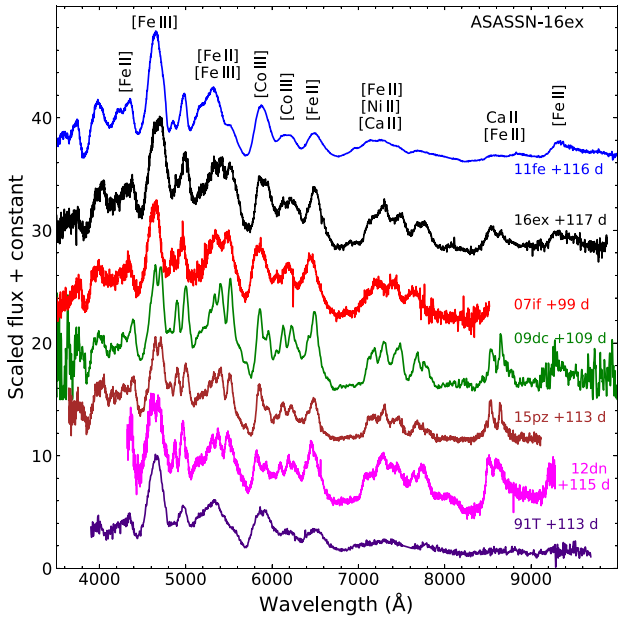

Figure 15. The spectrum of ASASSN-16ex at + 117 d is compared with those of other well-studied SNe Ia.

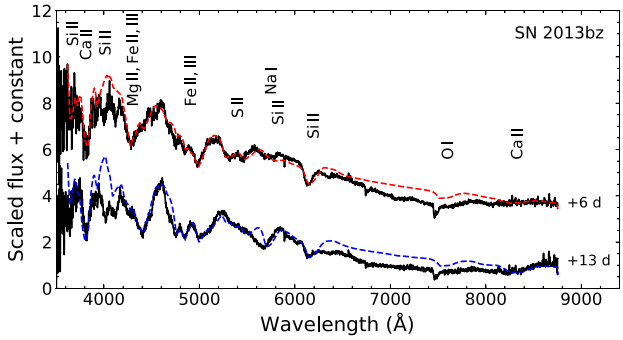

Figure 16. The synthetic spectra generated using the SYN++ code are compared with the observed spectra of SN 2013bz.

ASASSN-16ex is less than in a normal SN Ia. In the red region beyond ∼ 6500 Å, features in ASASSN-16ex are more pronounced compared with normal SN 2011fe and luminous SN 1991T. There are a number of similarities between the spectrum of ASASSN-16ex and 09dc-like SNe, which include (i) double-peaked [Fe II] + [Fe III] complex at ∼ 5400 Å, where the strength of [Fe III] 4700 Å appears lower relative to [Fe II] + [Fe III]; (ii) strong [Fe II] at ∼ 6500 Å; (iii) a broad absorption trough with a flat bottom around 6700–7000 Å; (iv) multiple emission peaks around 7000–7900 Å; (v) sharp emission peaks at ∼ 8500 Å.

5.5 SYN++ synthetic model spectra

Spectra of SN 2013bz at +6 and +13 d are compared with the synthetic spectra generated using the SYN++ code (Fisher 2000; Thomas, Nugent & Meza 2011) and plotted in Fig. 16. The observed spectrum at + 6 d matches the synthetic spectrum with a photospheric velocity (v_{ph}) of 10 500 km s^{-1} and blackbody temperature (T_{BB}) of 11 000 K. The species used are marked. The spectrum at

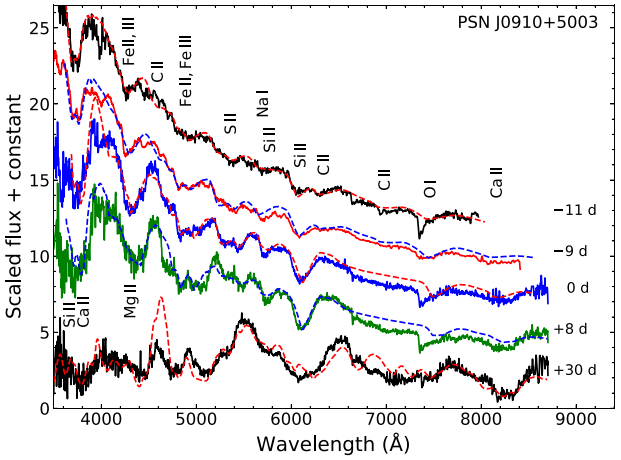

Figure 17. The synthetic spectra generated using the SYN++ code are compared with the observed spectra of PSN J0910 + 5003.

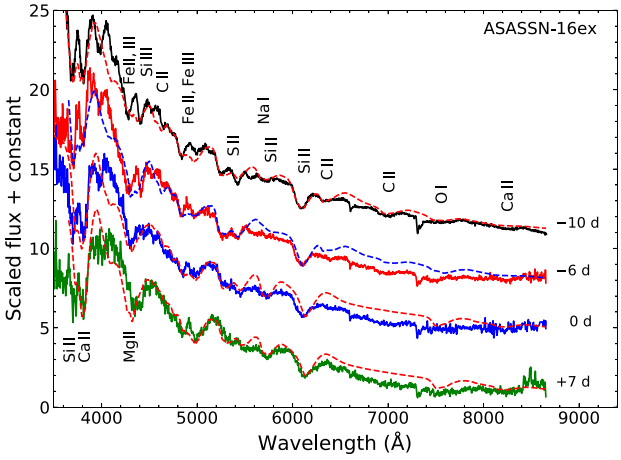

Figure 18. The synthetic spectra generated using the SYN++ code are compared with the observed spectra of ASASSN-16ex.

+ 13 d matches with similar T_{BB} and species but with a lower v_{ph} of 10 200 km s^{-1}.

Spectra of PSN J0910+5003 at −11, −9, 0, +8, and + 30 d are matched with the synthetic spectrum and plotted in Fig. 17. The synthetic spectrum at −11 d is produced using v_{ph} = 14 500 km s^{-1} and T_{BB} = 15 000 K. Ions used are marked in the figure. The synthetic spectrum at −9 d is reproduced with similar species, v_{ph} = 13 500 km s^{-1} and T_{BB} = 14 300 K. For the maximum and one-week post-maximum phase, we used v_{ph} = 11 700 and 11 500 km s^{-1}, T_{BB} = 13 000 and 11 500 K, respectively. Species used are similar to the −9 d spectrum; C II is not included. The synthetic spectrum at + 30 d has v_{ph} = 10 000 km s^{-1} and T_{BB} = 8000 K. It includes species of Si II, Ca II, Fe II, Ni II, and Co II.

Spectra of ASASSN-16ex at −10, −6, 0, and + 7 d are matched with the synthetic spectrum and plotted in Fig. 18. The synthetic spectrum at −10 d is generated using v_{ph} = 12 500 km s^{-1} and T_{BB} = 15 000 K. Species used are marked. The observed spectrum of ASASSN-16ex at −6 d matches the synthetic spectrum with similar parameters and species used at −10 d. The synthetic spectra at maximum and one week post-maximum phase have lower v_{ph}

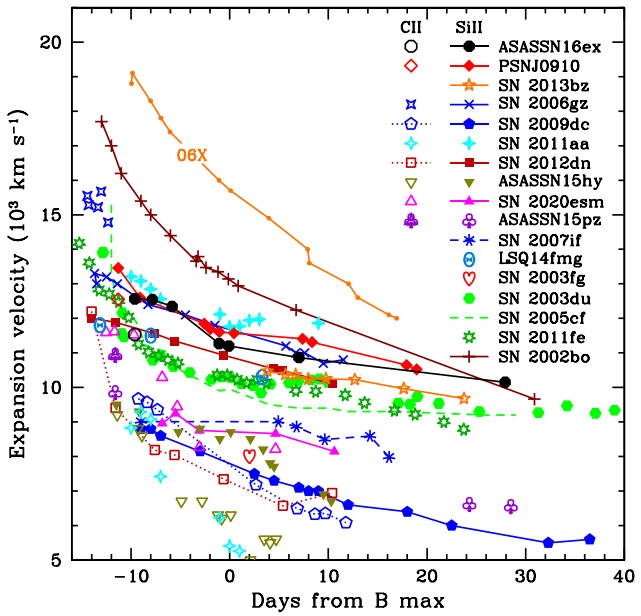

Figure 19. Photospheric velocity evolution measured using Si II λ6355 absorption line for SN 2013bz, PSN J0910 + 5003, and ASASSN-16ex compared with other well-studied SNe Ia. The velocity of the C II λ6580 line is also displayed for PSN J0910 + 5003 and ASASSN-16ex, along with other SNe Ia.

(11 200 km s^{-1} and 11 000 km s^{-1}) and T_{BB} (14 500 and 14 000 K). Both include species of O I, Na I, Mg II, Si II, S II, Ca II, Fe II, and Fe III.

5.6 Velocity and spectral parameters

The photospheric velocities of SN 2013bz, PSN J0910 + 5003, and ASASSN-16ex estimated using the absorption minimum of Si II λ6355 are plotted in Fig. 19, along with other well-studied SNe Ia for comparison. The velocity evolution of SN 2013bz is similar to that of normal event SN 2003du. The velocity evolution of PSN J0910 + 5003 and ASASSN-16ex is similar to that of SN 2006gz and the early evolution of SN 2011aa. The carbon λ6580 line detected in the early phase (∼−10 d) is found to have ∼ 1000 km s^{-1} lower velocity than the Si II line in both PSN J0910 + 5003 and ASASSN-16ex. This could be due to the clumping/line-of-sight effect (Parrent et al. 2011).

Normal SNe Ia are characterized by a pair of Si II λ5972 and Si II λ6355 features near the maximum phase. SNe Ia can be categorized and studied based on the various spectroscopic parameters derived from these lines, such as EWs (Branch et al. 2006) and strength ratio $\mathcal{R}_{Si}$ (Nugent et al. 1995), the photospheric velocity measured from the Si II λ6355 line (Wang et al. 2009b), and its gradient (Benetti et al. 2005). We measured these parameters for SN 2013bz, PSN J0910 + 5003, and ASASSN-16ex, and listed them in Table 7. All three SNe belong to normal velocity (NV: Wang et al. 2009b) and low velocity gradient (LVG: Benetti et al. 2005) subgroups. SN 2013bz and ASASSN-16ex fall in the shallow silicon (SS) subgroup, while PSN J0910 + 5003 is near the boundary of the SS and core normal (CN) subgroups of SNe Ia (Branch et al. 2006).

Table 7. Spectroscopic parameters of SN 2013bz, PSN J0910 + 5003, and ASASSN-16ex.

Parameter[a]	13bz	PSN	16ex
1. v_{ph} (km s^{-1})	10 500 ± 600	11 600 ± 200	11 200 ± 400
2. $\dot{v}_{Si}$ (km s^{-1} d^{-1})	40 ± 3	31 ± 3	50 ± 4
3. EW (Si II λ5972 Å)	11 ± 2	20 ± 2	16 ± 2
4. EW (Si II λ6355 Å)	30 ± 3	83 ± 8	60 ± 6
5. $\mathcal{R}_{Si}$	0.34 ± 0.03	0.37 ± 0.04	0.32 ± 0.03
6. Spectroscopic class[b]	LVG	LVG	LVG
7. Spectroscopic class[c]	SS	SS/CN	SS
8. Spectroscopic class[d]	NV	NV	NV

Notes. [a] Near *B* max, [b]Benetti et al. (2005), [c]Branch et al. (2006), [d]Wang et al. (2009b).

6 DISCUSSION AND SUMMARY

SN 2013bz, PSN J0910 + 5003, and ASASSN-16ex were classified as 09dc-like objects using their early spectra (Ochner et al. 2013; Tomasella et al. 2015, 2016; Piascik & Steele 2016). We have conducted a detailed photometric and spectroscopic study of these objects to investigate their properties further. Among these, SN 2013bz is a slow-declining, luminous event with a decline-rate parameter of $\Delta m_{15}(B)_{true} = 0.92 \pm 0.04$. Its photometric and spectral characteristics are similar to those of normal SNe Ia, while PSN J0910+5003 and ASASSN-16ex are similar to 09dc-like SNe Ia. The light curves of both PSN J0910 + 5003 and ASASSN-16ex are very broad relative to normal events. Their decline-rate parameters ($\Delta m_{15}(B)_{true}$ = 0.70 ± 0.05 and 0.73 ± 0.03) are similar to those of 09dc-like SNe Ia. Further, ASASSN-16ex is very blue and bright in the UV bands. The absolute luminosities of SN 2013bz, PSN J0910 + 5003, and ASASSN-16ex are on the higher side of normal SNe Ia. Their *B*-band peak absolute magnitudes are estimated as −19.61 ± 0.20 mag, −19.44 ± 0.20 mag, and −19.78 ± 0.20 mag, respectively.

The peak bolometric luminosities for these objects are derived as log L_{bol}^{max} = 43.38 ± 0.07, 43.26 ± 0.07, and 43.40 ± 0.06 erg s^{-1}, respectively. The mass of ^{56}Ni synthesized in the explosion of these events is estimated as 0.96 ± 0.24 $M_\odot$, 0.89 ± 0.24 $M_\odot$, and 1.2 ± 0.32 $M_\odot$, respectively. The contribution of the UV flux to the bolometric luminosity for ASASSN-16ex is estimated to be 22 per cent at *B* maximum. The late-phase spectrum of ASASSN-16ex, ∼ four months after maximum light, also looks very similar to those of 09dc-like SNe Ia.

The positions of SN 2013bz, PSN J0910 + 5003, and ASASSN-16ex, along with known 09dc-like objects and a sample of SNe Ia from Hicken et al. (2009), in the *luminosity–width relation* diagram of Phillips et al. (1999) are shown in Fig. 20. Phillips et al. (1999) used SNe Ia in the range 0.85 < $\Delta m_{15}(B)_{true}$ < 1.7. Since then, the sample of SNe Ia has increased significantly, with a higher number of objects at both the higher and lower luminosity ends. Normal SNe Ia are suggested to follow this relation.

09dc-like SNe Ia are now known to have a large dispersion in their luminosity. SNe 2003fg, 07if, 09dc, and LSQ14fmg were exceptionally bright (Howell et al. 2006; Yamanaka et al. 2009; Scalzo et al. 2010; Yuan et al. 2010; Silverman et al. 2011; Taubenberger et al. 2011; Hsiao et al. 2020), while ASASSN-15hy had a lower luminosity (Lu et al. 2021). Other SNe 2006gz, 12dn, ASASSN-15pz, 20esm, 20hvf, and 21zny have luminosities in between (Hicken et al. 2009; Maeda et al. 2009; Chakradhari et al. 2014; Chen et al. 2019; Taubenberger et al. 2019; Jiang et al. 2021; Dimitriadis et al. 2022, 2023). Their decline rate ranges from

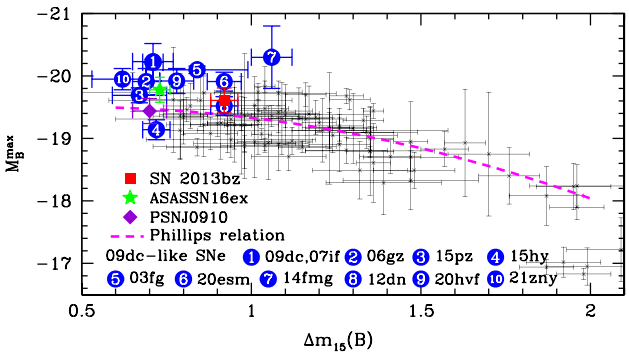

Figure 20. Positions of SN 2013bz, PSN J0910 + 5003, and ASASSN-16ex are shown in the *luminosity–width relation* diagram of Phillips et al. (1999) along with the known 09dc-like objects and a sample of type Ia SNe from Hicken et al. (2009).

0.62 ± 0.09 (SN 2021zny: Dimitriadis et al. 2023) to 1.06 ± 0.06 (LSQ14fmg: Hsiao et al. 2020). Except for LSQ14fmg, all 09dc-like objects have $\Delta m_{15}(B)$ lower than a typical SN Ia. From Fig. 20, it is clear that, with a slower decline, PSN J0910 + 5003 and ASASSN-16ex lie towards the region occupied by 09dc-like objects and are moderately luminous. SN 2013bz falls in the region of normally luminous SNe Ia.

One of the characteristics seen in 09dc-like SNe is the appearance of a delayed *I*-band maximum. Timings of the *I*-band peak relative to the *B*-band peak for 09dc-like SNe, 91T, and normal SNe are listed in Table 5. PSN J0910 + 5003 has a delayed *I*-band peak (6 d), similar to other objects showing the most delayed *I*-band peaks, e.g. SN 2006gz (6 d), SN 2011aa (7 d), and ASASSN-15hy (7 d). However, ASASSN-16ex does not show a delayed *I*-band peak.

Kasen (2006) suggested that a double-peak appearance in the NIR light curves can be regarded as a direct consequence of ejecta stratification and concentration of IGEs in the central regions. The secondary maximum results due to the ionization evolution of IGEs in the ejecta and transition from a doubly ionized to a singly ionized (Fe III to Fe II) state (Pinto & Eastman 2000; Kasen 2006). Brighter SNe are expected to have a more pronounced and delayed secondary maximum, but this may vary depending on the amount and mixing of ^{56}Ni, stable Fe/metallicity, and abundance of calcium (Kasen 2006). Folatelli et al. (2010) suggested that mixing has the most significant effect on the strength of the secondary maximum, and it can transform double-peak morphology into a single peak, as seen in the 09dc-like SNe.

Ashall et al. (2021) suggested that full mixing in the ejecta should cause a prominent *H*-band break in the NIR spectrum, which is not seen during the early post-maximum phase in 09dc-like SNe; instead, it is delayed by ∼ 1–2 months. The delayed appearance of the *H*-band break indicates that ^{56}Ni resides in the very inner layers. Vigorous mixing would bring ^{56}Ni to the outermost region of the ejecta. However, the decay of surface ^{56}Ni was not a good fit for the short-duration early excess of SN 2020hvf (Jiang et al. 2021).

Explaining the bolometric light curve of 09dc-like SNe requires a higher ^{56}Ni mass, suggesting an ejecta mass in excess of the Chandrasekhar mass (Scalzo et al. 2010). In the SD scenario, differentially rotating WDs can have masses greater than the Chandrasekhar mass (Yoon & Langer 2005), offering a possible progenitor for 09dc-like SN Ia (Howell et al. 2006). However, Pfannes et al. (2010a), Pfannes, Niemeyer & Schmidt (2010b), Hachinger et al. (2012), and Fink et al. (2018) show that the explosion energetics/burning products do not match well with this model. The deflagration model of differentially rotating WDs produces SNe Iax-like events. The explosion in the detonation/delayed detonation is very powerful, the velocities of IMEs are significantly high, and most of the materials are burned to IGEs with just a small portion remaining unburned, contrary to what is seen in 09dc-like SNe Ia.

Ejecta–CSM interaction has also been proposed as an alternative energy source to power these events. In this scenario, a 09dc-like SN is suggested to be a thermonuclear explosion in an enshrouded shell/envelope (Khokhlov, Mueller & Hoeflich 1993; Hoeflich & Khokhlov 1996) of C/O-rich materials with which the supernova ejecta interacts. The conversion/reprocessing of kinetic energy/shock interaction energy acts as an additional source (Hicken et al. 2007; Scalzo et al. 2010; Taubenberger et al. 2013; Noebauer et al. 2016; Hsiao et al. 2020; Ashall et al. 2021; Lu et al. 2021).

The signature of ejecta–CSM has been observed in some 09dc-like SNe Ia. In SN 2012dn, the excess NIR luminosity was interpreted as due to the presence of CSM dust (Yamanaka et al. 2016; Nagao, Maeda & Yamanaka 2017). Short-duration pulse-like early excess emission in SN 2020hvf (Jiang et al. 2021), SN 2021zny (Dimitriadis et al. 2023), and SN 2022ilv (Srivastav et al. 2023) within a few hours of the supernova explosion was modelled as an interaction of SN ejecta with the CSM close to the progenitor (see also Maeda et al. 2023). However, the absence of narrow emission lines in the spectra of 09dc-like SNe Ia indicates the CSM to be H/He-poor.

The origin of CSM is not well understood. Yamanaka et al. (2016) and Nagao et al. (2017) suggest an SD scenario. The merger of two WDs in the DD scenario gives a high ejecta mass suitable for 09dc-like SNe Ia (Hicken et al. 2007), and naturally explains the absence of H/He features. During the disruption, a WD merging with another WD can form a dense envelope of C/O-rich materials. However, the physics of merging WDs needs to be understood: whether it is able to explain SNe Ia (Hoeflich & Khokhlov 1996; Fryer et al. 2010; Shen et al. 2012; Moll et al. 2014; Raskin et al. 2014) or whether it will result in an accretion-induced collapse (Saio & Nomoto 1985). Hsiao et al. (2020), Ashall et al. (2021), and Lu et al. (2021) suggest a 'core-degenerate' scenario (Kashi & Soker 2011), where the explosion takes place in a degenerate C/O core enveloped by an AGB star. However, interaction signatures, e.g. bright X-ray emission, UV late-time rebrightening, narrow H/He lines, etc., have not been observed.

SN 2011aa was found to be the slowest declining Type Ia event, with photometric evolution similar to 09dc-like objects. However, it was neither overluminous nor showed narrow spectral features, as are seen in 09dc-like objects (Dutta et al. 2022). The photometric properties of PSN J0910+5003 match closely with 09dc-like objects, while the spectral lines in PSN J0910 + 5003 are broad, similar to those of SN 2011aa (refer to Section 5.4). Early velocity evolution of PSN J0910 + 5003 is also similar to that of SN 2011aa (refer to Fig. 19). Dutta et al. (2022) have shown that events like SN 2011aa could be explained by the violent merger of white dwarfs.

A strong C II feature is seen in the early spectra of PSN J0910 + 5003 and ASASSN-16ex at ∼−10 d. The presence of strong carbon lines is a characteristic of 09dc-like objects. Though carbon is seen in early spectra of a good fraction of normal SNe Ia, it generally disappears soon (Parrent et al. 2011; Folatelli et al. 2012; Silverman & Filippenko 2012). Some 09dc-like objects have shown carbon features extending up to the maximum/post-maximum phase, e.g. SN 2009dc (Taubenberger et al. 2011), SN 2012dn (Chakradhari et al. 2014; Parrent et al. 2016; Taubenberger et al. 2019), LSQ14fmg (Hsiao et al. 2020), ASASSN-15hy (Lu et al. 2021), SN 2020hvf (Jiang et al. 2021), SN 2020esm (Dimitriadis et al. 2022), SN 2021zny (Dimitriadis et al. 2023), and SN 2022ilv (Srivastav et al.

2023). The C II lines seen around ∼−10 d in PSN J0910 + 5003 and ASASSN-16ex faded speedily, similarly to SN 2006gz. The origin of the carbon is not fully understood. The strong C II lines in 09dc-like SNe suggest a large amount of unburned material in the SN ejecta. This supports a model with an extended envelope. SN 2020esm had a nearly pure C/O atmosphere during the first few days of the explosion. The large amount of carbon in the envelope is swept up by the ejecta, giving rise to strong/persistent C II features (Taubenberger et al. 2013; Noebauer et al. 2016; Dimitriadis et al. 2022). Maeda et al. (2023) suggest that the sequence of SN 2020hvf, 2012dn, and 2020esm/2009dc could be connected to an increase in the C/O-rich envelope, resulting in increasing strength of C II and decreasing velocity of Si II as found by Ashall et al. (2021) for a sample of 09dc-like SNe Ia.

The presence of carbon may also help in dust formation in these objects (Maeda et al. 2023). Pre-existing dust or CO/dust formation may cause a fast decline in the light curves (Taubenberger et al. 2013, 2019; Chakradhari et al. 2014; Yamanaka et al. 2016; Nagao et al. 2017; Hsiao et al. 2020). Early fast decline, starting within ∼ 1–3 months of the *B* maximum, was seen in SN 2012dn (Chakradhari et al. 2014; Yamanaka et al. 2016; Taubenberger et al. 2019), ASASSN-15pz (Chen et al. 2019), and LSQ14fmg (Hsiao et al. 2020), while a fast decline in the late phase was seen in SN 2006gz (Maeda et al. 2009), SN 2009dc (Silverman et al. 2011; Taubenberger et al. 2013), and SN 2020esm (Dimitriadis et al. 2022). No signature of fast decline is seen in the light curves of PSN J0910 + 5003 and ASASSN-16ex until the last available data point (∼ 4 months).

The shell/envelope configuration helps to explain the low ejecta velocity and slow evolution (Noebauer et al. 2016). Most 09dc-like SNe Ia, e.g. SN 2003fg, 07if, 09dc, 20esm, ASASSN-15pz, 15hy, were found to have very low ejecta velocities: their velocities near the maximum phase are below 10 000 km s^{-1}, while SNe 2006gz, 12dn, and LSQ14fmg were found to have higher velocities (refer to Fig. 19). Both PSN J0910 + 5003 and ASASSN-16ex have velocity evolution similar to SN 2006gz. Along with high-velocity features, SN 2020hvf had a relatively high ejecta velocity. Jiang et al. (2021) suggest that there could be different origins of 09dc-like SNe with different velocities.

All 09dc-like SNe Ia can be placed in the normal velocity (NV) subgroup of Wang et al. (2009b). They have a lower gradient in their velocity evolution, falling into the LVG subgroup of the Benetti et al. (2005) classification scheme. PSN J0910 + 5003 and ASASSN-16ex both fall in the NV and LVG subgroups. The strength of Si II λ5972, λ6355 lines in 09dc-like SNe Ia is found to be weak. The relative strength of these lines is temperature-sensitive (Nugent et al. 1995). Hotter events have a weaker Si II λ5972 line. At lower temperatures, Fe II/Co II line blanketing increases the strength of Si II λ5972, while at higher temperatures Fe III/Co III line blanketing washes out this feature. 09dc-like SNe are UV blue and bright during the early/maximum phase, making their photosphere hotter, giving a weaker Si II λ5972 line. 09dc-like SNe mostly fall in the 'shallow silicon' (SS) subgroup of the Branch et al. (2006) classification. The Si II λ5972, λ6355 lines appear weak in the maximum-phase spectrum of ASASSN-16ex; hence, spectroscopically, it can be categorized in the SS subgroup, while PSN J0910 + 5003 falls near the boundary of the SS and CN subgroups. The velocity evolution of SN 2013bz is similar to that of SN 2003du. The Si II λ5972 line is shallower, falling in the 'shallow silicon' (SS) subgroup. It has a normal velocity (NV) at maximum and a low velocity gradient (LVG) in the post-maximum phase.

In this work, we have presented detailed photometric and spectroscopic analyses of three supernovae: SN 2013bz, PSN J0910+5003, and ASASSN-16ex. SN 2013bz is a slow-declining, luminous event with photometric/spectral characteristics similar to those of normal SNe Ia, while most of the photometric/spectroscopic properties of PSNJ 0910 + 5003 and ASASSN-16ex are similar to those of 09dc-like SNe Ia. The combined data for these objects allow us to explore and compare various astrophysical parameters of normal and peculiar SNe Ia and help us understand differences in their characteristics. Adding well-studied new members to the family of peculiar SNe Ia will enhance our knowledge of these objects and SNe Ia diversity.

ACKNOWLEDGEMENTS

We thank the anonymous referee for providing constructive comments, which improved the presentation of this work. ST and NKC are thankful to the Director and Dean of IIA, Bengaluru, for the local hospitality and facilities provided. We are thankful to the staff at CREST and IAO for their assistance during the observations and to all the observers of the 2-m HCT (IAO-IIA), who kindly provided part of their observing time for supernova observations. We have used public data in the *Swift* data archive. This work has made use of the NASA Astrophysics Data System (ADS), NASA/IPAC Infrared Science Archive (IRSA), and the NASA/IPAC Extragalactic Database (NED), which is operated by Jet Propulsion Laboratory, California Institute of Technology, under contract with the National Aeronautics and Space Administration. We acknowledge the use of the Weizmann Interactive Supernova Data Repository (WISeREP), maintained by the Weizmann Institute of Science computing center.

DATA AVAILABILITY

The photometric and spectroscopic data presented in this work will be made available by the corresponding author upon request.

REFERENCES

Altavilla G. et al., 2004, MNRAS, 349, 1344
Anupama G. C., Sahu D. K., Jose J., 2005, A&A, 429, 667
Arnett W. D., 1982, ApJ, 253, 785
Ashall C. et al., 2021, ApJ, 922, 205
Benetti S. et al., 2005, ApJ, 623, 1011
Bessell M. S., Castelli F., Plez B., 1998, A&A, 337, 321
Branch D., 1992, ApJ, 392, 35
Branch D. et al., 2006, PASP, 118, 560
Breeveld A. A., Landsman W., Holland S. T., Roming P., Kuin N. P. M., Page M. J., 2011, in McEnery J. E., Racusin J. L., Gehrels N.eds, American Institute of Physics Conference Series Vol. 1358, Gamma Ray Bursts 2010. American Institute of Physics (AIP), Online, p. 373
Brown P. J., Milne P., 2016, The Astronomer's Telegram, 9035, 1
Brown P. J. et al., 2009, AJ, 137, 4517
Brown P. J. et al., 2010, ApJ, 721, 1608
Brown P. J. et al., 2012, ApJ, 753, 22
Brown P. J., Breeveld A. A., Holland S., Kuin P., Pritchard T., 2014a, Ap&SS, 354, 89
Brown P. J. et al., 2014b, ApJ, 787, 29
Burns C. R. et al., 2011, AJ, 141, 19
Cardelli J. A., Clayton G. C., Mathis J. S., 1989, ApJ, 345, 245
Chakradhari N. K., Sahu D. K., Srivastav S., Anupama G. C., 2014, MNRAS, 443, 1663
Chakradhari N. K., Sahu D. K., Anupama G. C., 2019, MNRAS, 487, 1886
Chen P. et al., 2019, ApJ, 880, 35
Ciabattari F., Mazzoni E., Petroni G., 2015, Central Bureau for Astronomical Telegrams TOCP, PSN J09100885 + 5003396
Conley A. et al., 2006, AJ, 132, 1707
Dimitriadis G. et al., 2022, ApJ, 927, 78

Dimitriadis G. et al., 2023, MNRAS, 521, 1162
Dutta A., Anupama G. C., Chakradhari N. K., Sahu D. K., 2022, ApJ, 938, L22
Filippenko A. V. et al., 1992, ApJ, 384, L15
Fink M., Kromer M., Hillebrandt W., Röpke F. K., Pakmor R., Seitenzahl I. R., Sim S. A., 2018, A&A, 618, A124
Firth R. E. et al., 2015, MNRAS, 446, 3895
Fisher A. K., 2000, PhD thesis, The University of Oklahoma
Folatelli G. et al., 2010, AJ, 139, 120
Folatelli G. et al., 2012, ApJ, 745, 74
Foley R. J. et al., 2018, MNRAS, 475, 193
Freedman W. L. et al., 2001, ApJ, 553, 47
Fryer C. L. et al., 2010, ApJ, 725, 296
Ganeshalingam M., Li W., Filippenko A. V., 2011, MNRAS, 416, 2607
Hachinger S., Mazzali P. A., Taubenberger S., Fink M., Pakmor R., Hillebrandt W., Seitenzahl I. R., 2012, MNRAS, 427, 2057
Hamuy M., Phillips M. M., Suntzeff N. B., Schommer R. A., Maza J., Smith R. C., Lira P., Aviles R., 1996, AJ, 112, 2438
Hayden B. T. et al., 2010, ApJ, 712, 350
Hicken M., Garnavich P. M., Prieto J. L., Blondin S., DePoy D. L., Kirshner R. P., Parrent J., 2007, ApJ, 669, L17
Hicken M. et al., 2009, ApJ, 700, 331
Hoeflich P., Khokhlov A., 1996, ApJ, 457, 500
Howell D. A. et al., 2006, Nature, 443, 308
Howerton S. et al., 2013, Central Bureau Electronic Telegrams, 3507
Hoyle F., Fowler W. A., 1960, ApJ, 132, 565
Hsiao E. Y. et al., 2020, ApJ, 900, 140
Iben Jr. I., Tutukov A. V., 1984, ApJS, 54, 335
Jha S. W., Maguire K., Sullivan M., 2019, Nature Astronomy, 3, 706
Jiang J.-a. et al., 2021, ApJ, 923, L8
Kasen D., 2006, ApJ, 649, 939
Kashi A., Soker N., 2011, MNRAS, 417, 1466
Khokhlov A. M., 1991, A&A, 245, L25
Khokhlov A., Mueller E., Hoeflich P., 1993, A&A, 270, 223
Kiyota S. et al., 2016, The Astronomer's Telegram, 9020, 1
Landolt A. U., 1992, AJ, 104, 340
Li W. et al., 2011, MNRAS, 412, 1441
Lira P. et al., 1998, AJ, 115, 234
Livio M., Mazzali P., 2018, Phys. Rep., 736, 1
Lu J. et al., 2021, ApJ, 920, 107
Maeda K., Kawabata K., Li W., Tanaka M., Mazzali P. A., Hattori T., Nomoto K., Filippenko A. V., 2009, ApJ, 690, 1745
Maeda K., Jiang J.-a., Doi M., Kawabata M., Shigeyama T., 2023, MNRAS, 521, 1897
Maoz D., Mannucci F., Nelemans G., 2014, ARA&A, 52, 107
Matteucci F., Greggio L., 1986, A&A, 154, 279
Matteucci F., Spitoni E., Recchi S., Valiante R., 2009, A&A, 501, 531
Mazzali P. A., Röpke F. K., Benetti S., Hillebrandt W., 2007, Science, 315, 825
Miller A. A. et al., 2020, ApJ, 902, 47
Milne P. A., Brown P. J., Roming P. W. A., Bufano F., Gehrels N., 2013, ApJ, 779, 23
Moll R., Raskin C., Kasen D., Woosley S. E., 2014, ApJ, 785, 105
Mould J. R. et al., 2000, ApJ, 529, 786
Nadyozhin D. K., 1994, ApJS, 92, 527
Nagao T., Maeda K., Yamanaka M., 2017, ApJ, 835, 143
Noebauer U. M., Taubenberger S., Blinnikov S., Sorokina E., Hillebrandt W., 2016, MNRAS, 463, 2972
Nomoto K., Kobayashi C., Tominaga N., 2013, ARA&A, 51, 457
Nugent P., Phillips M., Baron E., Branch D., Hauschildt P., 1995, ApJ, 455, L147
Ochner P., Tomasella L., Pastorello A., Benetti S., Cappellaro E., Turatto M., 2013, Central Bureau Electronic Telegrams, 3513
Pakmor R., Kromer M., Taubenberger S., Springel V., 2013, ApJ, 770, L8
Parrent J. T. et al., 2011, ApJ, 732, 30
Parrent J. T. et al., 2012, ApJ, 752, L26
Parrent J. T. et al., 2016, MNRAS, 457, 3702
Pastorello A. et al., 2007, MNRAS, 376, 1301
Pereira R. et al., 2013, A&A, 554, A27
Perlmutter S. et al., 1999, ApJ, 517, 565
Pfannes J. M. M., Niemeyer J. C., Schmidt W., Klingenberg C., 2010a, A&A, 509, A74
Pfannes J. M. M., Niemeyer J. C., Schmidt W., 2010b, A&A, 509, A75
Phillips M. M., 1993, ApJ, 413, L105
Phillips M. M., Lira P., Suntzeff N. B., Schommer R. A., Hamuy M., Maza J., 1999, AJ, 118, 1766
Piascik A. S., Steele I. A., 2016, The Astronomer's Telegram, 9023, 1
Pinto P. A., Eastman R. G., 2000, ApJ, 530, 757
Poole T. S. et al., 2008, MNRAS, 383, 627
Raskin C., Kasen D., Moll R., Schwab J., Woosley S., 2014, ApJ, 788, 75
Reindl B., Tammann G. A., Sandage A., Saha A., 2005, ApJ, 624, 532
Richmond M. W., Smith H. A., 2012, Journal of the American Association of Variable Star Observers (JAAVSO), 40, 872
Riess A. G. et al., 1998, AJ, 116, 1009
Riess A. G. et al., 1999, AJ, 118, 2675
Roming P. W. A. et al., 2005, Space Sci. Rev., 120, 95
Ruiter A. J., 2020, in Barstow M. A., Kleinman S. J., Provencal J. L., Ferrario L., eds, IAU Symposium. White Dwarfs as Probes of Fundamental Physics: Tracers of Planetary, Stellar and Galactic Evolution, Vol. 357, Cambridge University Press, p. 1
Ruiter A. J., Belczynski K., Sim S. A., Seitenzahl I. R., Kwiatkowski D., 2014, MNRAS, 440, L101
Saio H., Nomoto K., 1985, A&A, 150, L21
Scalzo R. A. et al., 2010, ApJ, 713, 1073
Schlafly E. F., Finkbeiner D. P., 2011, ApJ, 737, 103
Shen K. J., Bildsten L., Kasen D., Quataert E., 2012, ApJ, 748, 35
Silverman J. M., Filippenko A. V., 2012, MNRAS, 425, 1917
Silverman J. M., Ganeshalingam M., Li W., Filippenko A. V., Miller A. A., Poznanski D., 2011, MNRAS, 410, 585
Silverman J. M. et al., 2012, MNRAS, 425, 1789
Soker N., 2019, New Astron. Rev., 87, 101535
Srivastav S. et al., 2023, ApJ, 943, L20
Stahl B. E. et al., 2020, MNRAS, 492, 4325
Tanikawa A., Nomoto K., Nakasato N., 2018, ApJ, 868, 90
Taubenberger S., 2017, Handbook of Supernovae, The Extremes of Thermonuclear Supernovae. Springer International Publishing, Cham, Switzerland, p. 317
Taubenberger S. et al., 2011, MNRAS, 412, 2735
Taubenberger S. et al., 2013, MNRAS, 432, 3117
Taubenberger S. et al., 2019, MNRAS, 488, 5473
Thomas R. C., Nugent P. E., Meza J. C., 2011, PASP, 123, 237
Tomasella L. et al., 2015, The Astronomer's Telegram, 8263, 1
Tomasella L. et al., 2016, The Astronomer's Telegram, 9024, 1
Turatto M., Benetti S., Cappellaro E., Danziger I. J., Della Valle M., Gouiffes C., Mazzali P. A., Patat F., 1996, MNRAS, 283, 1
Turatto M., Benetti S., Cappellaro E., 2003, in Hillebrandt W., Leibundgut B.eds, Proc. ESO/MPA/MPE Workshop, From Twilight to Highlight: The Physics of Supernovae. Springer, Berlin, p. 200, preprint (astro-ph/0211219)
Vinkó J. et al., 2012, A&A, 546, A12
Wang B., 2018, Research in Astronomy and Astrophysics, 18, 049
Wang X., Wang L., Pain R., Zhou X., Li Z., 2006, ApJ, 645, 488
Wang X. et al., 2009a, ApJ, 697, 380
Wang X. et al., 2009b, ApJ, 699, L139
Webbink R. F., 1984, ApJ, 277, 355
Whelan J., Iben I. Jr, 1973, ApJ, 186, 1007
Woosley S. E., Kasen D., 2011, ApJ, 734, 38
Woosley S. E., Weaver T. A., 1994, ApJ, 423, 371
Yamanaka M. et al., 2009, ApJ, 707, L118
Yamanaka M. et al., 2016, PASJ, 68, 68
Yoon S. C., Langer N., 2005, A&A, 435, 967
Yuan F. et al., 2010, ApJ, 715, 1338

This paper has been typeset from a TEX/LATEX file prepared by the author.